

A Smartphone-Based Method for Assessing Tomato Nutrient Status through Trichome Density Measurement

SHO UEDA^{1*} XUJUN YE²

¹United Graduate School of Agricultural Sciences, Iwate University, Morioka, Iwate, 020-8550, Japan.

²Faculty of Agriculture and Life Science, Hirosaki University, Hirosaki, Aomori, 036-8560, Japan.

Abstract

Early detection of fertilizer-induced stress in tomato plants is crucial for timely crop management interventions and yield optimization. Conventional optical methods detect fertilizer stress in young leaves with difficulty. This study proposes a novel, noninvasive technique for quantifying the density of trichomes—elongated hair-like structures found on plant surfaces—on young leaves using a smartphone. This method exhibits superior detection latency, enabling earlier and more accurate identification of fertilizer stress in tomato plants. Our approach combines augmented reality technology and image processing algorithms to analyze smartphone images of a specialized measurement paper. This measurement paper is applied to a tomato leaf to transfer trichomes onto its adhesive surface. The captured images are then processed through a pipeline involving region of interest extraction, perspective transformation, and illumination correction. Trichome detection and spatial distribution analysis of these preprocessed images yield a robust density metric. We validated our method through experiments on hydroponically grown tomatoes under varying fertilizer concentrations. Using leave-one-out cross-validation (LOOCV), our model achieves a mean area under the precision-recall curve of 0.824 and a receiver operating characteristic curve of 0.641 for predicting additional fertilization needs. Based on LOOCV, quantitative analysis revealed a strong relationship between trichome density and explanatory variables, including nitrate ion concentration, explaining 62.48% of the variation ($R^2 = 0.625$). The predicted and actual trichome densities were strongly correlated ($r = 0.794$). This straightforward and cost-effective method overcomes the limitations of traditional techniques, demonstrating the potential of using smartphones for practical plant nutrition diagnosis.

Keywords: Tomato, tomato leaf, fertilizer stress, trichome, smartphone, computer vision, machine learning, precision agriculture, digital agriculture

1 Introduction

Tomato (*Solanum lycopersicum*), a vegetable that is widely cultivated worldwide, is influenced by various environmental factors that affect its production and quality. The nutrient status of plants, one of the most crucial factors influencing tomato yield, is an important consideration in tomato production. Therefore, accurately assessing plant nutrient status is essential for maintaining high tomato yields. Techniques have been developed to analyze the constituents of fertilizers in soil, media, and nutrient solutions, aiming to estimate the amount of nutrients absorbed by plants [1, 2]. Additionally, researchers have developed invasive methods to analyze plant nutrients [3, 4]. Moreover, noninvasive techniques such as visual inspection and sensor-based monitoring are available for assessing plant traits.

*Corresponding author : Sho Ueda

Morphological changes can serve as valuable indicators for nutritional analysis, particularly in the context of environmental stressors such as drought and nutrient deficiencies. With respect to drought stress, Klepper et al. conducted an observational study and reported that cotton stem diameter, leaf water potential, and relative leaf water content are closely related to the net radiation above the plant canopy [5]. Wakamori et al. optically analyzed the wilting of tomato leaves and changes in stem diameter in an observational study and demonstrated a correlation between these parameters[6]. In terms of nutrient stress, Padilla et al. provided a comprehensive review of techniques for monitoring the nitrogen status of vegetable crops via optical methods [7]. Locascio et al. and Coltman demonstrated a causal relationship between the fertilization rate and tomato yield in interventional studies[8, 9]. Tei et al. reported a causal relationship between the fertilization rate and tomato leaf area in an interventional study[10]. These findings emphasize that environmental stressors alter the vegetative and reproductive growth patterns observed in plants.

The ability to detect and examine these modifications allows for a more sophisticated understanding of the nutrient levels of plants and their responses to varying environmental conditions. Leaf area and chlorophyll content, which are related to leaf color and spectrum, are commonly used as indicators of the adaptive response of plants to fertilizer stress. dela Torre et al. reviewed various optical indices, leaf area, biomass, and other phenotypes for estimating rice yield via remote sensing[11]. Cartelat et al. demonstrated that optically assessed contents of leaf polyphenols and chlorophyll in wheat can be used as indicators of nitrogen deficiency[12]. Padilla et al. reported that chlorophyll meters and canopy reflectance sensors serve as sensitive indicators of N status across a wide range of vegetable crops[13]. These methods have led to the development of a diagnostic framework based on the relationships among fertilizer application, phenotypic expression, and yield outcomes. Color and spectral data analysis of plant canopies enables predictions of plant health and productivity. These predictions utilize wide-area imagery from satellites, aircraft, and drones combined with data collected from in-field sampling stations. The aforementioned optical observation techniques, which utilize reflected light from the plant body, effectively address the need for noninvasive and digital monitoring of phenotypes [7].

Furthermore, techniques for detecting fertilizer stress in tomatoes have been extensively researched. Tables 1 and 2 present a comprehensive comparison of various noninvasive methods for early detection of fertilizer stress in tomato plants. We focused on studies that employed interventional experiments with varying fertilizer levels and used noninvasive measurement techniques on tomatoes. Priority was given to methods that utilized digital measurement tools and enabled measurements as close to the growth point as possible for early stress detection. As shown in Table 1, although these methods may appear equally effective at first glance, the complexity of data processing (visualization, modeling, and interpretation) after measurement must be considered, which varies considerably depending on the selected phenotypic indicator and sensor type.

Moreover, in terms of detection latency, which refers to the delay between the onset of fertilizer stress and its detection, evaluating phenotypic indicators based on the metabolic mechanisms of tomato plants is crucial. Tomatoes exhibit apical growth, where cell differentiation occurs at the top of the plant, and differentiated organs move downward as the plant grows. Considering this mechanism, measuring phenotypic indicators near the shoot apical meristem could lead to earlier and more accurate detection of fertilizer stress. However, as shown in Table 2, existing studies primarily utilize "fully expanded leaves" or even the entire plant as a phenotypic indicator for chlorophyll meters, visible-near infrared spectroscopy, fluorescence spectroscopy, stem diameter measurement, and leaf area measurement. A "fully expanded leaf" is generally considered the 3rd to 5th compound leaf from the apex, excluding the apical meristem and leaf primordia, and has reached its final size and shape. However, a universally accepted definition of a fully expanded leaf does not exist, and its specific characteristics are as follows: The precise distance from the apical meristem may vary depending on factors such as plant species, cultivar,

Table 1: Comparison of Noninvasive Methods for Detection of Fertilizer Stress in Tomato Plants

Method	Phenotypic Indicator	Instrumentation	Conditions to Avoid	Data Complexity
Proposed Method	Trichome density	Digital camera	Direct sunlight	2D image array
Leaf Chlorophyll Content [14]	Chlorophyll a and b content	Chlorophyll meter	Direct sunlight	Scalar value
Visible-Near Infrared Spectroscopy [14]	Multiple biochemical components	VIS-NIR spectrometer	Direct sunlight	1D spectral array
Fluorescence Spectroscopy [15]	Multiple fluorescent compounds	Fluorescence spectrometer	Bright light	1D spectral array
Leaf Area [16]	Leaf area	Ruler	Withering	Scalar value
Stem Diameter [17]	Stem diameter	Caliper	Withering	Scalar value

* This table includes studies that met the following criteria: noninvasive measurement, tested on tomatoes, interventional experiments with varying fertilizer levels. Priority was given to methods with digital measurements and those enabling measurements near the growth point for early stress detection.

Table 2: Measurement Sites and Sensitivity for Early Detection

Method	Leaf Age or Plant Part for Early Detection	Sensitivity to Fertilizer Stress
Proposed Method	15 cm from shoot meristem (not fully expanded leaf)	$R = 0.79$, $mPR^d = 0.82$, $mROC^d = 0.64$
Leaf Chlorophyll Content [14]	Fully expanded leaf ^a	Correlated ^b
Visible-Near Infrared Spectroscopy [14]	Stem area 34 cm below fully expanded leaf ^a	Correlated ^b
Fluorescence Spectroscopy [15]	Fully expanded leaf ^a	$p < 0.05$, $n = \text{not specified}^c$
Leaf Area [16]	All leaves on the plant	Correlated ^b
Stem Diameter [17]	The canopy height on the main stem ^a	$p < 0.05$, $n = 72^c$

^a Measurement location not specified in the original study.

^b Sensitivity to fertilizer stress was not quantitatively assessed in the original study; however, a correlation was visually observed in the presented figures.

^c Specific sensitivity indicator was not provided in the original study.

^d mPR and mROC represent the mean area under the precision-recall curve and the mean area under the receiver operating characteristic curve, respectively (see equations 10 and 11). These metrics evaluate the performance of the model in determining the need for additional fertilization.

growth stage, and environmental conditions. Therefore, the context of each study must be considered when interpreting the term "fully expanded leaf." Consequently, studies in the literature identifying the phenomenon of fertilizer stress are lacking. This scarcity is especially true in the assessment of young tomato leaves, with the definition of "young leaves" itself being subject to variation.

2 Related Work

Gianquinto et al. conducted a study using a multispectral radiometer positioned directly above the tomato plant canopy to investigate the correlation between light reflectance, chlorophyll concentration, and total Kjeldahl nitrogen content in an intervention study of fertilizer application. By employing this noncontact arrangement, measurements were conducted without physically interacting with the leaves. They discovered a linear relationship between optical reflectance and chlorophyll concentration; however, no such linear relationship was identified between the optical reflectance and total Kjeldahl nitrogen content [18]. Similarly, Padilla et al. directly observed the most recently fully expanded leaves via an optical leaf-clip chlorophyll meter (Konica Minolta, SPAD-502). A linear relationship was observed between optical observations and the nitrogen nutrition index under conditions of a flattened leaf surface structure [14]. In both investigations, the absence of any barriers along the path of light between the observing device and the plant leaves is assumed, highlighting a gap between the specifications of diagnostic equipment for farmers and the current state of research and development.

However, in contrast to other crops, tomatoes have numerous trichomes, which are small projections or hair-like structures, on the surface of their leaves (Figure 1). Trichomes are densely concentrated on young, actively growing leaves and sparsely distributed on older leaves [19]. The presence of surface microstructures, such as trichomes, on plant bodies is known to



Figure 1: Many trichomes-small projections or hair-like structures-are present on the surface of tomato leaves.

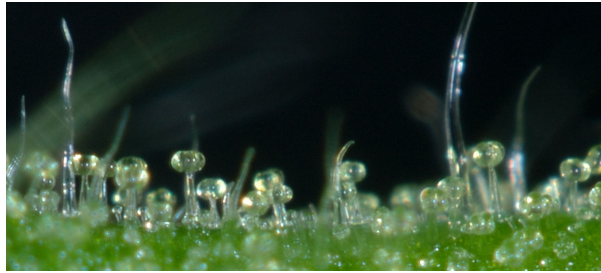


Figure 2: Type VI trichomes on the tomato plant surface.

considerably affect their appearance [20–22]. Given their high density on young tomato leaves, it is plausible that trichomes may influence the effectiveness of optical sensing techniques used to assess the nutrient status of tomato plants. Consequently, the presence of trichomes should be considered a potential practical limitation when optical sensing techniques are used on young tomato leaves to evaluate fertilizer stress. However, current methodologies do not adequately address the impact of trichomes on the optical sensing techniques used for the rapid assessment of tomato plant nutrient status.

Counting trichomes, which are abundant on young tomato leaves, is not easily achievable via visual means. Manually counting trichomes via a microscope is one of the few methods available for quantifying their density. Trichomes are abundant on young tomato leaves and are not easily distinguishable by visual means alone. The lack of a specialized device for assessing trichome density may have hindered progress in this area of research.

The chlorophyll content, which is correlated with leaf color, is a widely used indicator of fertilizer stress in plants. However, it is not the only marker. Trichomes have also been identified as potential indicators of fertilizer stress, as they contribute to plant defense against pests by responding to fertilizer stress and altering plant density [23, 24]. Various types of trichomes can be observed on the surface of tomato leaves, most of which are short, hair-like trichomes and trichomes with large, spherical cells at their tips (known as type VI trichomes, Figure 2) [25]. The glandular head of type VI trichomes is connected to the stalk cell at the base by fragile cell walls [26]. This structural arrangement allows the glandular part to easily detach from the leaf surface upon physical stimulation. The mucilage within the glandular part is known to inhibit pest activity.

Researchers have observed multiple instances where trichomes respond to fertilizer stress [23, 24, 27]. For example, Barbour et al. revealed an inverse relationship between fertilizer application, leaf nitrogen content, and trichome density [23]. Similarly, Hoffland et al. reported a positive correlation between the leaf carbon:nitrogen ratio and trichome density [24]. In contrast, Leite et al. presented data indicating that trichome density increased over time when less fertilizer was used compared with that of conventional farming methods [28]. Despite these find-

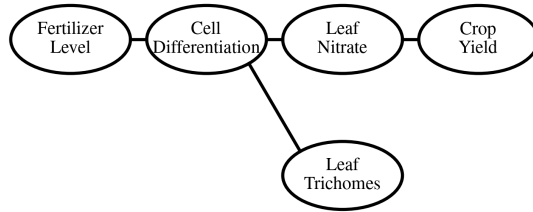


Figure 3: **Hypothesized relationships between fertilizer level, cell differentiation, leaf nitrate content, number of leaf trichomes, and crop yield for tomato plants, serving as the conceptual framework for the study.**

ings, most previous studies have focused on investigating trichome density within a biological context, with limited exploration of techniques to observe trichome density in agricultural production settings without advanced laboratory equipment. This limitation highlights the need for further research to develop practical methods for assessing trichome density in real-world agricultural environments.

To address this gap, the present study focused on tomato leaf trichomes and explored their potential as indicators for assessing the nutrient status of tomato plants. As depicted in Figure 3, our main hypothesis is that leaf trichome density is influenced by fertilizer level. These findings suggest its potential as an additional indicator of plant nutrient status in conjunction with traditional fertilizer stress markers such as the leaf nitrate content. To this end, a tool for assessing trichome density must be developed. The identification of distinct items within a particular setting containing several objects inside the visual field is commonly considered a computer vision problem [29, 30]. Given this context, we hypothesized that the use of cameras could convert the challenge of measuring trichome density to an analogy of an object detection problem.

Recently, the increasing prevalence of smartphones, with their advanced computational capabilities, high-resolution cameras, and internet access, has spurred the development of proof-of-concept agricultural technologies. These technologies have a wide range of applications, including farm management, crop monitoring, and pest and disease diagnosis, as highlighted in a comprehensive review by Mendes et al. [31]. For example, Neumann et al. demonstrated a method for classifying diseases in sugar beet leaves using images captured directly with a smartphone camera [32], and Johannes et al. similarly classified wheat diseases via direct leaf images [33]. Furthermore, Li et al. successfully achieved early detection of late blight in tomato leaves using measurement sheet[34]. In their study, images of a measurement sheet used to analyze leaf volatiles were captured via a smartphone. Inspired by these advancements, our study aimed to investigate the feasibility of using smartphones as a cost-effective tool for measuring trichome density. These parameters can serve as predictive indicators of tomato plant nutrient status.

3 Materials and Methods

3.1 Development of a Smartphone-Based Trichome Density Measurement Method

3.1.1 Design of a simple kit for collecting trichomes from tomato leaves

In this study, we designed a straightforward kit to measure the density of type VI glandular trichomes on tomato leaves. This kit comprises custom-made measurement paper crafted from inkjet-printable cardstock and cellophane tape (NICHIBAN, CT-18), enabling cost-effective measurements (Figure 4). This paper contains augmented reality (AR) markers, enabling the distance of objects within captured images to be precisely measured. Additionally, there is a



Figure 4: A smartphone was used to capture an image of the diagnostic kit.

12 mm \times 12 mm opening in the center of the paper. A piece of cellophane tape is affixed to the back of the paper, covering this opening. This tape is used to extract trichomes from the surface of tomato leaves.

Optimizing a technique that involves the use of cellophane tape for trichome extraction allows the creation of a highly cost-efficient kit. Although recent advances in sophisticated object detection algorithms have utilized complex neural networks, these neural networks typically demand high-speed parallel processing, considerably increasing computational costs. Our approach, which uses cellophane tape for trichome extraction, circumvents the need for such intensive computational resources and enables the use of less computationally demanding algorithms for trichome detection. Thus, this approach reduces the overall cost of the assessment process, making it more economically viable.

The purpose of this diagnostic kit is to meet the technological progress needs in agricultural production areas that lack access to laboratory-level experimental facilities. Therefore, to minimize the number of components required for measurement, the kit is specifically designed to allow for dual manual operation. The measuring paper is held in one hand, whereas the smartphone is operated in the other hand (Figure 4). The statistical model accounts for the variability in the results caused by varying optical conditions among shots. The kit is designed to prioritize user friendliness as a minimum viable product in lean startup methodology for manufacturing and software development, enabling the measurement of trichome density without requiring technical expertise [35, 36]. This technology is well suited for practical application in the field because of its simplicity and cost-effectiveness (Figure 5).

3.1.2 Proposed concept of the tomato cultivation support framework

This kit is designed to empower farmers to assess the additional fertilization needs of their tomato plants based on trichome density and receive fertilization recommendations. The proposed framework involves a four-step process. First, trichomes are sampled from tomato leaves via adhesive cellophane tape on measurement paper. Second, a smartphone is used to capture an image of the measurement paper with the transferred trichomes. Third, the captured image is analyzed to determine trichome density, which serves as an indicator of the degree of fertilizer stress. Finally, on the basis of the analyzed trichome density, the system provides a fertilization recommendation to the farmer, guiding their decision on whether additional fertilization is

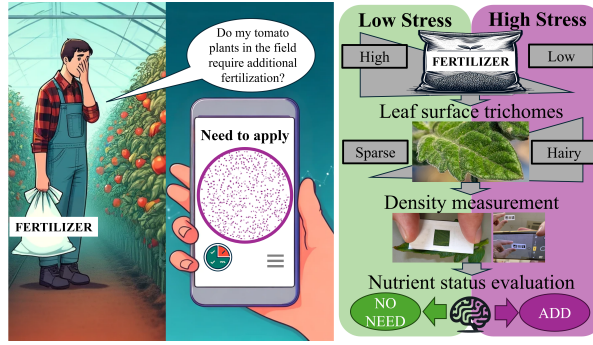


Figure 5: **Proposed concept of the tomato cultivation support framework.**

necessary.

3.1.3 Overview of the trichome detection image processing pipeline

This study implemented an image processing pipeline for calculating trichome density. Instead of using deep learning models for direct image processing, tabular data analysis was chosen. Although deep learning often requires substantial computational resources, this architecture leverages the inherent simplicity and reduced dimensionality of tabular data, enabling the use of computationally lighter models. This method effectively minimizes computational costs while bolstering quantitative model interpretation, thereby improving the reliability and interpretability of the results for agricultural applications.

To avoid data leakage, an image processing pipeline was developed using images obtained from preliminary experiments. This approach ensured that the model development and evaluation processes remained independent and unbiased.

The image processing pipeline comprises three main stages. The preprocessing stage involves extracting metadata in the exchangeable image file format (EXIF) embedded in the image files, identifying AR markers within the images, applying homography transformations for image alignment, and adjusting for variations in lighting conditions. This preprocessing stage also includes binarizing images to segment trichomes and applying noise removal filtering algorithms to enhance trichome visibility.

In the feature extraction stage, we focused on identifying trichomes in the images, specifically targeting type VI glandular trichomes, owing to their unique morphology. Furthermore, AR markers were utilized to convert pixel counts to relative distances, enabling accurate distance estimation. The final stage, density calculation, involves calculating the trichome density from images captured under various environmental conditions and camera settings, each associated with distinct EXIF data. Algorithm 1 presents an outlined function of the trichome density computation process using our custom-developed measurement kit. The image processing procedures described above were executed via the software specifications outlined in Table 3.

3.1.4 Image preprocessing: AR marker detection, illumination correction, and noise reduction

The first step of the developed image processing pipeline is to read EXIF data from the image files. This metadata contains valuable information about the environmental conditions and camera settings at the time of image capture. By analyzing aspects such as exposure time and ISO speed ratings, we can gain a comprehensive understanding of the variations in imaging conditions and their potential impacts on trichome density measurements.

To measure the absolute scale and orientation of the captured images, we incorporated AR

Algorithm 1 Trichome density analysis process

Require: *image*: Image file

Ensure: *density*: Nearest neighbor density

Ensure: *expTime*: Exposure time from EXIF data

Ensure: *iso*: ISO speed from EXIF data

Ensure: *openingPx*: Pixel count of measurement paper opening

```
1: function READEXIFANDLOAD(image)
2:   Read EXIF data from image
3:   expTime, iso  $\leftarrow$  Extract from EXIF data
4:    $I(x, y) \leftarrow$  Convert image to the array
5:   return  $I(x, y), expTime, iso$ 
6: end function
7: function DETECTMARKERS( $I(x, y)$ )
8:   Detecting AR markers in  $I(x, y)$ 
9:   markers  $\leftarrow$  Extract coordinates from markers
10:  openingPx  $\leftarrow$  Calculate the opening pixel count
11:  return openingPx, markers
12: end function
13: function APPLYHOMOGRAPHY( $I(x, y), markers$ )
14:  Apply homography transform to  $I(x, y)$ 
15:  return  $I_{trans}(x, y)$ 
16: end function
17: function CORRECTILLUM( $I(x, y)$ )
18:  Apply illumination correction to  $I(x, y)$ 
19:  return  $I_{corr}(x, y)$ 
20: end function
21: function REMOVE_NOISE( $I(x, y)$ )
22:  Apply noise removal to  $I(x, y)$ 
23:  return  $I_{clean}(x, y)$ 
24: end function
25: function SEGMENTTRICHOMES( $I(x, y)$ )
26:  Apply watershed segmentation to  $I(x, y)$ 
27:  return trichomes
28: end function
29: function CALCDENSITY(trichomes)
30:  density  $\leftarrow$  Calculate nearest neighbor density
31:  return density
32: end function
```

Main Execution

```
33:  $I(x, y), expTime, iso \leftarrow$  READEXIFANDLOAD(image)
34: openingPx, markers  $\leftarrow$  DETECTMARKERS( $I(x, y)$ )
35:  $I_{trans}(x, y) \leftarrow$  APPLYHOMOGRAPHY( $I(x, y), markers$ )
36:  $I_{corr}(x, y) \leftarrow$  CORRECTILLUM( $I_{trans}(x, y)$ )
37:  $I_{clean}(x, y) \leftarrow$  REMOVE_NOISE( $I_{corr}(x, y)$ )
38: trichomes  $\leftarrow$  SEGMENTTRICHOMES( $I_{clean}(x, y)$ )
39: density  $\leftarrow$  CALCDENSITY(trichomes)
```

Table 3: Versions of Libraries and Operating System Used

Operating System/Library	Version
Ubuntu	22.04.2 LTS
opencv-contrib-python	4.6.0.66
imbalanced-learn	0.12.0
lightgbm	3.3.5
shap	0.43.0
ExifRead	3.0.0

markers into our image processing pipeline. These markers enabled us to determine the trichome density of the captured images. For AR marker detection, we utilized the ArUco module from the OpenCV library (version 4.6.0.66) [37].

The AR marker detection algorithm employs a simple, nonrecursive approach, as the development of AR technology was not the primary focus of this study. The process involves image preprocessing, where the captured image is converted to grayscale and then binarized via Otsu’s method to enhance marker visibility under various lighting conditions. We used a predefined "ArUco dictionary", `DICT_4X4_250`. This dictionary offers a balance between the number of unique markers and detection robustness. Finally, the OpenCV function `cv2.aruco.detectMarkers()` is used to identify the ArUco markers in the preprocessed image.

The complete algorithm is presented in Algorithm 2.

Algorithm 2 AR marker detection

Require: I : Input image

Ensure: C : Detected marker corners

Ensure: ids : Detected marker IDs

- 1: **function** TOGRAY(img)
Convert img to grayscale **return** grayscale image
- 2: **end function**
- 3: **function** BINARIZE(img)
Apply Otsu’s binarization **return** binary image
- 4: **end function**
- 5: **function** GETDICT($type$)
Create ArUco dictionary **return** dictionary
- 6: **end function**
- 7: **function** GETPARAMS
Create detector parameters **return** parameters
- 8: **end function**
- 9: **function** DETECTM($img, dict, params$)
Detect ArUco markers **return** corners and IDs
- 10: **end function**

Main Execution

- 11: $G \leftarrow$ TOGRAY(I)
 - 12: $B \leftarrow$ BINARIZE(G)
 - 13: $D \leftarrow$ GETDICT($DICT_4X4_250$)
 - 14: $P \leftarrow$ GETPARAMS
 - 15: $C, ids \leftarrow$ DETECTM(B, D, P)
-

Following AR marker detection, we apply homography transformation to correct perspective distortion in images. This distortion is caused by positional and orientational variations in the measurement paper relative to each camera captured. The homography transformation adjusts the images as though the camera and the measurement paper were parallel. This process involves using the coordinates of the four corners of a region on the measurement paper, obtained from detecting AR markers as reference points to estimate a perspective transformation matrix. By applying this transformation, we ensure that the images are standardized for accurate trichome density analysis, regardless of slight variations in camera positioning during image capture.

After applying the homography transformation, we implemented an illumination correction procedure to address nonuniform lighting conditions across the acquired images. This step is essential for maintaining consistency in trichome detection, regardless of ambient lighting variations during image acquisition.

Our approach uses a flat field correction technique [38], which involves several preprocessing steps. Initially, all the images are resized to a standardized dimension of 1000 pixel \times 1000 pixel to ensure uniform processing. We subsequently apply an averaging filter with a kernel size of 50 pixel \times 50 pixel to generate a smoothed version of the image, representing the overall illumination pattern.

The correction is mathematically described by the following equation:

$$C = \frac{R \times m}{F} \quad (1)$$

where C denotes the corrected image, R represents the original (precorrection) image, m is the average luminance of the original image, and F is the smoothed image representing the illumination pattern. The details of this correction are presented in Algorithm 3.

Following the illumination correction, we implemented a noise removal step. It is widely recognized that noise in images can harm detection accuracy in object detection tasks. Therefore, as a preprocessing measure, we employed morphological opening, a type of morphological transformation. This technique is particularly effective in eliminating small-scale noise and artifacts while preserving the overall shape and size of larger objects of interest and is especially efficient in reducing background noise. The opening operation was performed via a 3×3 square structuring element with all the elements set to 1, which was applied in a single iteration. The size of the structuring element was determined with consideration of the target glandular trichomes, which are approximately 60 μm [26] in diameter, ensuring that the element was smaller than the objects of interest.

3.1.5 Feature extraction: trichome identification and density analysis

Following noise removal, a segmentation procedure based on the watershed algorithm was implemented to identify individual trichomes. This method detects boundary surfaces that separate contours in the image. The watershed algorithm was chosen because of its suitability for rule-based segmentation on the basis of the distinctive appearance of trichomes, offering a computationally efficient solution. Although deep learning-based segmentation can often achieve high accuracy, it typically requires substantial computational resources, often necessitating the use of devices with advanced parallel processing capabilities, such as graphics processing units, to be integrated into the computer system. In contrast, the watershed algorithm, which is a traditional image-processing technique, generally operates with lower computational costs and can often perform effectively on standard computer hardware, such as central processing units. This characteristic is particularly important for our application, as it ensures that the tomato nutrient diagnostic kit remains cost-effective for farmers, aligning with our goal of developing accessible and practical tools for agriculture.

During this analysis, we identified individual trichomes on the adhesive surface of the cellophane tape. Type VI trichomes are characterized by their spherical heads [39], fragile layer

Algorithm 3 Illumination correction

Require: R : Precorrection image

Ensure: C : Corrected image

```
1: function APPLYBLUR( $image, kw, kh$ )
2:    $w \leftarrow$  width of  $image$ 
3:    $h \leftarrow$  height of  $image$ 
4:    $output \leftarrow$  new image of size  $w \times h$ 
5:   for  $y \leftarrow 0$  to  $h - 1$  do
6:     for  $x \leftarrow 0$  to  $w - 1$  do
7:        $sum \leftarrow 0$ 
8:        $count \leftarrow 0$ 
9:       for  $j \leftarrow -kh/2$  to  $kh/2$  do
10:        for  $i \leftarrow -kw/2$  to  $kw/2$  do
11:           $nx \leftarrow x + i$ 
12:           $ny \leftarrow y + j$ 
13:          if  $0 \leq nx < w$  and  $0 \leq ny < h$  then
14:             $sum \leftarrow sum + image[ny][nx]$ 
15:             $count \leftarrow count + 1$ 
16:          end if
17:        end for
18:      end for
19:       $output[y][x] \leftarrow sum/count$ 
20:    end for
21:  end for
22:  return  $output$ 
23: end function
24: function CALCULATEAVERAGELUMINANCE( $image$ )
25:    $sum \leftarrow 0$ 
26:    $count \leftarrow 0$ 
27:   for each pixel  $p$  in  $image$  do
28:      $sum \leftarrow sum + p$ 
29:      $count \leftarrow count + 1$ 
30:   end for
31:   return  $sum/count$ 
32: end function
```

Main Execution

```
33:  $F \leftarrow$  APPLYBLUR( $R, 50, 50$ )
34:  $m \leftarrow$  CALCULATEAVERAGELUMINANCE( $R$ )
35:  $C \leftarrow \frac{R \times m}{F}$ 
```

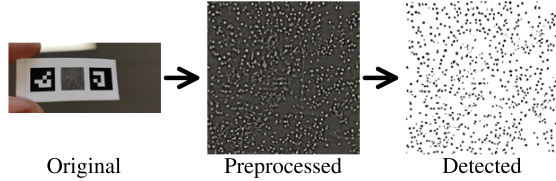


Figure 6: **Example of image data preprocessing and object detection.**

aiding head detachment [26], and relatively large average diameter of approximately $60\ \mu\text{m}$ [26] compared with other trichomes. We distinguished type VI glandular trichomes via physical and optical filtering on the basis of specific properties. Trichome identification assumes that the quantity of glandular trichomes on the leaf surface is substantial, as previously mentioned.

In this paper, we utilize the term "trichomes" to describe the contours of detected objects based on the following criteria:

- A detachable layer must exist, allowing peeling with cellophane tape;
- The object should be larger than a pixel, with a minimum size of approximately $10\ \mu\text{m}$, and must be detectable in the image;
- The lower limit of the shape factor within the survey area is defined as the 1st quartile minus 1.5 times the interquartile range;
- The upper limit of the shape factor within the survey area is defined as the 3rd quartile plus 1.5 times the interquartile range;
- An object's shape should more closely resemble a sphere than a prolate ellipsoid, with the circularity exceeding a defined lower limit;
- The perimeter of the object falls within a specified range, defined by a lower and upper limit;
- The area of the object lies within a specified range, defined by a lower and upper limit.

The contours detected through segmentation yield centroid points, denoted as in Equation 2. These points exist within a two-dimensional space and are represented via the pixel coordinates of the image. Figure 6 shows the image processing steps performed up to this point, including preprocessing and object detection.

The watershed segmentation process yields a set of detected contours, from which we extract centroid points. These points are represented in a two-dimensional space corresponding to the pixel coordinates of the image. The set of centroids is denoted as P , as defined in Equation 2.

$$P = p_i \in \mathbb{R}^2 \mid i = 1, 2, \dots, N \quad (2)$$

where p_i represents the i -th centroid point in the two-dimensional real space \mathbb{R}^2 , and N is the total number of detected contours. Each point p_i can be expressed as (x_i, y_i) , where x_i and y_i are the horizontal and vertical pixel coordinates, respectively.

The detailed process of trichome identification, including the criteria and thresholds used for filtering, is presented in Algorithm 4. This algorithm encapsulates the key steps and decision-making process involved in distinguishing type VI glandular trichomes from other objects in the image. Figure 6 shows the image processing steps performed up to this point, including preprocessing and object detection.

The density was computed for the centroid points denoted as P in Equation 2. We employed the nearest neighbor distance (NND) method, as described in Equation 3 [40], to quantify the

Algorithm 4 Trichome identification

Require: I : Preprocessed image

Ensure: P : Set of trichome centroid points

```
1: function ISVALIDTRICHOME( $contour, C_{th}, P_l, P_h, A_l, A_h$ )
2:    $C \leftarrow$  CALCULATECIRCULARITY( $contour$ )
3:    $P \leftarrow$  CALCULATEPERIMETER( $contour$ )
4:    $A \leftarrow$  CALCULATEAREA( $contour$ )
5:   if  $C < C_{th}$  then
6:     return false
7:   end if
8:   if  $P < P_l$  or  $P > P_h$  then
9:     return false
10:  end if
11:  if  $A < A_l$  or  $A > A_h$  then
12:    return false
13:  end if
14:  return true
15: end function
16: function CALCULATEALLMETRICS( $contours$ )
17:   Calculate circularity, perimeter, and area for all contours
18:   return  $C_{all}, P_{all}, A_{all}$ 
19: end function
20: function CALCULATECENTROIDPOINT( $contour$ )
21:   Calculate the centroid point  $(x, y)$  of the  $contour$ 
22:   return  $(x, y)$ 
23: end function
```

Main Execution

```
24:  $contours \leftarrow$  WATERSHEDSEGMENTATION( $I$ )
25:  $P \leftarrow \emptyset$ 
26:  $C_{all}, P_{all}, A_{all} \leftarrow$  CALCULATEALLMETRICS( $contours$ )
27:  $C_{th} \leftarrow 1.5 \times Q1(C_{all})$ 
28:  $P_l, P_h \leftarrow 1.5 \times Q1(P_{all}), 1.5 \times Q3(P_{all})$ 
29:  $A_l, A_h \leftarrow 1.5 \times Q1(A_{all}), 1.5 \times Q3(A_{all})$ 
30: for each  $contour$  in  $contours$  do
31:   if ISVALIDTRICHOME( $contour, C_{th}, P_l, P_h, A_l, A_h$ ) then
32:      $centroidPoint \leftarrow$  CALCULATECENTROIDPOINT( $contour$ )
33:      $P \leftarrow P \cup \{centroidPoint\}$ 
34:   end if
35: end for
```

spatial distribution of these points. The NND method involves measuring the distance between each point and its nearest neighbor within the set.

$$NND = \frac{1}{n} \sum_{i=1}^n d(p, q) \quad (3)$$

In this equation, $d(p, q)$ represents the Euclidean distance between point p and its closest neighboring point q . The NND is then calculated by averaging these distances over the total number of contours n present in the image. Efficiently computing the nearest neighbors of each point is crucial, especially when many points are dealt with. A brute-force approach, where distances between all point pairs are calculated, would have a computational complexity of $O(nd)$, where n is the number of data points and d is the dimensionality. This "big O" notation, $O(nd)$, describes how the execution time of the algorithm increases as the input size (n, d) increases[41]. In this case, $O(nd)$ means that the execution time increases linearly with the number of points and the dimensionality. Therefore, the brute-force approach can become computationally expensive as the number of points increases. To address this issue, we utilized a k-dimensional tree algorithm, which organizes the points in a space-partitioning data structure that allows for rapid nearest neighbor queries. This algorithm effectively reduces the computational complexity to $O(d \log n)$ [42], meaning that the execution time grows linearly with the dimensionality but only logarithmically with the number of points. This logarithmic growth makes the k-d tree algorithm much more efficient than the brute-force approach, especially for large datasets. This algorithm is particularly suitable for our two-dimensional image analysis ($d = 2$) with many trichome centroids. The detailed implementation of the NND calculation is presented in Algorithm 5.

The NND serves as an inverse indicator of contour density, with higher values denoting sparse arrangements and lower values signifying denser groupings. Glandular type VI trichomes are susceptible to detachment from leaf surfaces because of factors such as insect infestations or physical abrasion. However, NND demonstrates superior robustness to such accidental detachment compared with conventional density indices, which are based on the object count per unit area. This robustness arises because NND represents density as a probability distribution, which enables it to maintain reliable estimates even when localized areas experience trichome detachment, provided that unaffected regions persist. Notably, the NND calculation requires the presence of at least two points. The appendix elucidates this concept through a simulation employing point cloud data generated via a Poisson process in two-dimensional space.

3.2 Evaluation of the New Method for Assessing the Nutrient Status of Tomato Plants

3.2.1 Selection of the cultivation method

A well-controlled cultivation experiment is essential for evaluating the proposed method for assessing the nutrient status of tomato plants with testability. This cultivation experiment aimed to measure phenotypes such as trichome density and leaf nitrate ion concentration and fruit yield under ideal conditions for tomato growth, minimizing the variability inherent in soil-based cultivation. Therefore, we opted for hydroponics rather than soil-based cultivation to circumvent the complexities associated with soil properties such as variations in soil composition and structure. These variations can lead to complexities in cultivation experiments, including inconsistent water retention, fertilizer dynamics, and potential for pest and disease outbreaks. This decision allowed for more precise control over nutrient availability and minimized potential confounding factors in our evaluation of fertilizer stress. This approach also enabled us to investigate the relationships between nutrient levels and plant responses more clearly in an ideal growth environment that approximates the optimal growth conditions found in some commercial cultivation systems.

Algorithm 5 Density analysis

Require: P : Set of trichome centroid points

Ensure: NND : nearest neighbor distance

```
1: function CALCNND( $P$ )
2:    $T \leftarrow$  BUILDKDTREE( $P$ )
3:    $S \leftarrow 0$ 
4:   for each  $p$  in  $P$  do
5:      $q \leftarrow$  FINDNN( $T, p$ )
6:      $d \leftarrow$  EUCLIDDIST( $p, q$ )
7:      $S \leftarrow S + d$ 
8:   end for
9:   return  $S/|P|$ 
10: end function
11: function BUILDKDTREE( $P$ )
12:   Construct a k-d tree from points  $P$ 
13:   return tree
14: end function
15: function FINDNN( $T, p$ )
16:   Find the nearest neighbor of  $p$  in tree  $T$ , excluding  $p$ 
17:   return nearest neighbor
18: end function
19: function EUCLIDDIST( $p, q$ )
20:    $dx \leftarrow p.x - q.x$ 
21:    $dy \leftarrow p.y - q.y$ 
22:   return  $\sqrt{dx^2 + dy^2}$ 
23: end function
```

Main Execution

```
24:  $NND \leftarrow$  CALCNND( $P$ )
```

Among various hydroponic techniques, we selected the deep water culture (DWC) method for its simplicity, minimal equipment requirements and ease of implementation in a randomized block design. In DWC, plant roots are fully submerged in nutrient solution within a production tank, which is aerated to sufficiently oxygenate the roots [43, 44]. This straightforward approach facilitates the relocation and replication of experimental units regardless of location, contributing to increased falsifiability. Moreover, DWC allows easy control of nutrient solution conditions at the individual plant level, making it suitable for randomized block designs.

3.2.2 Tomato growth conditions in hydroponic culture

The tomato cultivar (TAKII SEED, Fruitica) was grown hydroponically via the DWC method described above in a greenhouse with heating at Hirosaki University, Japan, with natural light as the sole source of illumination. The greenhouse was heated using a greenhouse heater controller (NEPON, HKC-253) set to 15 °C. Ventilation was provided via a greenhouse ventilation controller (Nihon Operator, JRM-102R) set to 25 °C. Fifteen-liter plastic buckets were used, with a planting density of 8 plants per 180 cm × 90 cm bed.

Within these buckets, the nutrient mixture was aerated and mixed by introducing air supplied by a blower (YASUNAGA, AP-40P). The air was divided into eight segments, each channeled through silicone tubing and dispersed into the nutrient solution. The use of air stones ensures proper mixing and oxygenation. The buckets were equipped with lids containing center holes for the tomato stems to prevent algae growth in the nutrient solution.

3.2.3 Fertilizer concentration settings

The nutrient solution was prepared via hydroponic fertilizer (OAT Agrio, Fertilizer Series SA), and maintained at three different total dissolved solids (TDS) concentrations to induce various levels of fertilizer stress:

- High concentration: 1500 ppm
- Intermediate concentration: 1000 ppm
- Low concentration: 500 ppm

This study employed an interventional research design to elucidate the causal relationship between fertilizer stress and tomato phenotypes. We set three fertilizer levels to investigate the presence or absence of intervention effects on tomato phenotypes and their dose-response relationships.

Given the lack of standardized cultivation protocols for controlling fertilizer levels in tomatoes via DWC, and considering the diverse objectives and cultivation conditions that individual growers optimize for, adopting a single universal value from prior research is inappropriate. This assertion underscores the importance of this study, which focuses on detecting fertilizer stress on the basis of plant phenotypes and ultimately utilizes this information to provide actionable fertilization recommendations. Nevertheless, previous studies have reported successful tomato cultivation via different closed hydroponic systems with a similar fertilizer composition to that in this study, where tomatoes thrived at an electrical conductivity (EC) of 1.1 dS m⁻¹ [45]. As this study managed nutrient levels via TDS, we converted this EC value to a TDS value on the basis of the standard nutrient solution composition (ppm and TDS) provided in the SA fertilizer composition table. This conversion indicated that an EC of 1.1 dS·m⁻¹ corresponds to approximately 500 ppm TDS.

Based on these findings, we set the low-concentration treatment at 500 ppm TDS. The intermediate- and high-concentration treatments were set at twice this level (1000 ppm) and three times this level (1500 ppm), respectively. Furthermore, to confirm that this range of

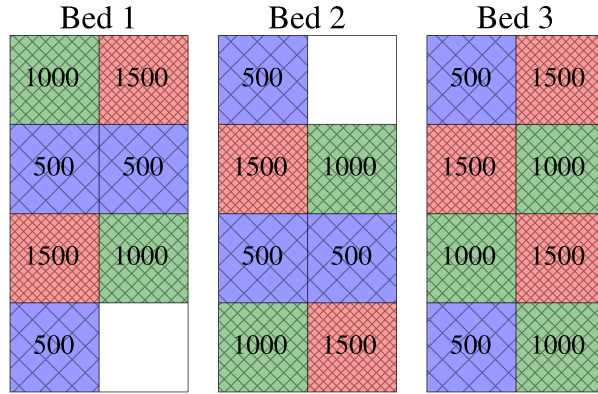


Figure 7: **Experimental layout with three different fertilizer levels (ppm) in a randomized block design.**

concentrations did not exert excessively adverse effects on tomato growth, we conducted preliminary cultivation experiments. The results revealed no visually identifiable growth defects or plant death at 500 ppm. Additionally, even at 1500 ppm, no apparent growth inhibition due to increased osmotic pressure was observed. These results confirmed the suitability of the selected fertilizer concentration range for the research objectives.

3.2.4 Experimental design and management

The fertilizer plots were arranged in a randomized block design, as shown in Figure 7. During the preliminary experiment, the tomato plants were initially cultivated in the vacant areas depicted in Figure 7. To evaluate the effects of fertilizer level on outcome variables, such as the concentration of nitrate ions in tomato leaves, the density of trichomes, and yield, this randomized block design was employed to minimize the potential impact of spatial variations in environmental factors [46].

Water was added to the buckets as needed when the nutrient solution water level decreased. Fertilizer was applied every two weeks, and nutrient solution concentrations were adjusted to maintain the desired TDS levels, which were measured via a TDS meter (EUTECH, PC-STestr35). The fertilizer used in the experiments closely matched the nutrient uptake ratios of the tomatoes, enabling the use of a closed hydroponic system without frequent nutrient solution replacement [45]. However, during the cultivation period, the system was not maintained as a completely closed system; nutrient solutions were replaced whenever they became cloudy because algae or root debris was present.

During the cultivation period, two plants were lost before the compound leaves were harvested, leaving 20 plants available for inclusion in the study. Furthermore, an additional two plants were lost by the end of the fruit harvesting period, resulting in 18 plants being available for harvest yield assessment.

3.2.5 Compound leaf sampling and trichome transfer

The experiment involved collecting compound leaves from tomato plants. A total of 40 compound leaf samples were collected during two separate harvesting sessions in March and April 2023. The sampling process followed a systematic approach to ensure consistency and minimize potential biases. The samples were processed sequentially in ascending order of the number of tomato plant samples. These sample numbers were randomly assigned to different fertilizer treatment levels as part of the randomized block design, ensuring that the sampling order was not biased by treatment level.

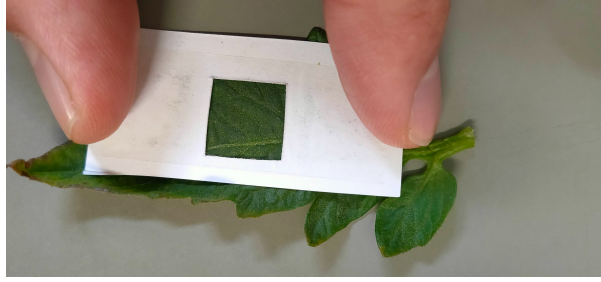


Figure 8: **Trichome transfer process from the leaflet surface to the measurement paper using cellophane tape.**

The compound leaves were sampled 15 cm below the apical meristem of each plant. If no suitable compound leaf was available at this position, the plant was temporarily skipped, allowing for further growth. The sampling process continued iteratively until all the plants had been sampled. For trichome density measurements, we selected all leaflets larger than the opening of the measurement paper from each compound leaf.

The number of measurement papers used corresponded to the number of selected leaflets per compound leaf: This approach allows for an accurate assessment of trichome density distribution across each leaflet. Prior to image capture, glandular trichomes were transferred from the leaflet surface to the measurement paper. Each leaflet was carefully affixed to the adhesive side of the cellophane tape (Figure 8) and gently pressed with a finger to ensure complete contact between the leaf surface and the tape. After the leaflet was removed, the cellophane tape with the transferred trichomes was photographed alongside the measurement paper via a smartphone camera.

3.2.6 Image acquisition and dataset preparation

The measurement paper was photographed via the native camera app on a smartphone (OPPO, Reno A). This device has a 16-megapixel camera featuring an F1.7 aperture and a CMOS sensor (Sony, IMX398). The camera supports autofocus functionality, allowing for sharp and clear images even under varying conditions. For our experiments, the camera mode was set to automatically adjust the exposure, ISO sensitivity, and focus, leveraging the device's built-in optimization algorithms.

To ensure a comprehensive dataset that accounts for various usage scenarios, we manually varied the distance and angle between the camera and the measurement paper. The distance from the camera sensor to the measurement paper ranged from 79 to 218 mm, simulating different user holding positions. The horizontal and vertical offset angles varied from -12.52 to 10.62 degrees and -9.04 to 8.13 degrees, respectively. This range of angles mimics slight misalignments that might occur during practical use of the kit. Furthermore, the measurement paper was positioned a sufficient distance from the background to ensure that the background was blurred and not clearly identifiable in the captured images.

The room used for photography had a north-facing window, which eliminated direct sunlight and provided diffuse natural light. The photographic sessions were conducted at different times of the day, with solar elevation angles ranging from -7.95 to 33.42 degrees. The smartphone's built-in white LED was activated for auxiliary lighting, and the measurement paper was additionally illuminated by oblique light from the ceiling's fluorescent light (as shown in Figure 4).

The image composition was carefully photographed to ensure that the measurement paper was centered in the frame.

Immediately after the images were captured, a preliminary analysis was conducted to verify the completeness of the image processing pipeline. All the measurement papers were checked to ensure that they could be included in the dataset. In cases where the analysis program

encountered exceptions, rephotography was performed to prevent bias due to missing information from the measurement paper during analysis. Consequently, this study focused exclusively on analyzing trichome density from images where AR markers could be detected.

The accuracy of AR marker detection was assumed to impact the results inconsiderably. This assumption was based on the practical consideration that the detection accuracy of AR markers and other 2D codes depend primarily on the library used and has already reached a practical level for applications. Moreover, in the event of an error, the kit user can rectify the problem by performing rephotography.

After the data collection and preprocessing steps, information from all the measurement papers was included in the final dataset, which comprised 6,855 images suitable for analysis. This comprehensive dataset encompasses a wide range of distances, angles, and lighting conditions and ensures that the developed model is trained and evaluated on a diverse set of scenarios, closely mimicking real-world usage of the kit.

3.2.7 Nitrate concentration measurement in tomato leaves

After the trichome density was measured, the tomato leaves were frozen with a refrigerant (HFO-1234ze) to facilitate cell wall structure breakdown and juice extraction. The leaves were placed in zippered plastic bags before freezing, allowing for the escape of moist air caused by refrigerant evaporation and preventing moisture accumulation within the bags. The frozen leaf samples were then thawed and mechanically pressed using pliers to extract the leaf juice. The extracted leaf juice was stored at -20°C for further analysis. After storage, the leaf juice was thawed and centrifuged to separate the solid and liquid components. After centrifugation, the clear supernatant was carefully collected, ensuring that no sediment particles were transferred. Electrophoresis buffer (Otsuka Electronics, α -AFQ133) was used to dilute the leaf juice 20-40 *times*. The diluted leaf juice was then filtered through a $0.45\ \mu\text{m}$ pore size syringe filter. The nitrate ion concentration in the filtered solution was measured via a capillary electrophoresis system (Agilent Technologies, 7100). A capillary tube with an internal diameter of $75\ \mu\text{m}$ and a length of 72 cm was utilized. The experimental parameters were as follows: buffer temperature, 25°C ; voltage, 20 kV; injection time, 4 s; injection pressure, 50 mbar; and detection wavelength, 350 nm. The nitrate ion concentration was determined via the absolute calibration method, where the measurements were based on a standard sample with a known concentration. The nitrate ion concentration was measured once for each compound leaf, yielding 40 scalar values. The nitrate ion concentration measurements were then combined with the trichome density measurements obtained from 6,855 images to create the dataset (Figure 9).

3.2.8 Assessment of tomato fruit harvest under experimental conditions

The fruit yield of the tomato plants was evaluated under experimental conditions. All fully ripened red fruits were harvested from each plant, stored at 5°C , and subsequently weighed.

3.3 Preliminary Data Analysis and Model Preparation

3.3.1 Configuration of the data analysis environment

The analytic environment was built using a Linux-based virtualization technology to ensure consistency and reproducibility of the analytical results across different computer systems, regardless of the specific hardware specifications. The analysis was conducted using Python [47] version 3.10. Table 3 provides a comprehensive list of the Python library versions and operating system versions utilized in this study. The `opencv-contrib-python`, `imbalanced-learn` [48], `lightgbm` [49], `shap` [50], and `ExifRead` [51] libraries were utilized for image processing, dataset preprocessing, machine learning model training, model interpretation, and metadata extraction from image data, respectively.

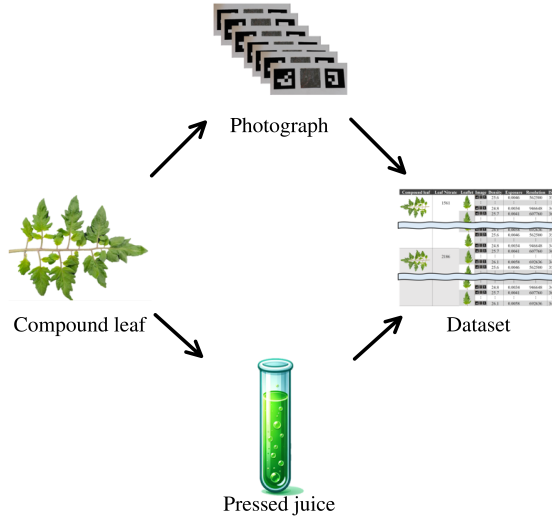


Figure 9: **Workflow from data acquisition to analysis.**

3.3.2 Statistical analysis of nitrate ion concentrations

We employed a series of nonparametric tests to statistically validate the observations of nitrate ion concentrations across different fertilizer levels. First, we used the Kruskal-Wallis test to examine the overall differences in distribution among the three fertilizer levels. Next, we conducted pairwise comparisons via Mann-Whitney U tests to assess the differences between each pair of fertilizer levels. To account for multiple comparisons, we applied the Bonferroni correction to the p values obtained from the Mann-Whitney U tests.

3.3.3 Multicollinearity and variable interaction assessment

Before building the model, we investigated the potential presence of multicollinearity and interaction effects among the predictor variables. Multicollinearity occurs when predictor variables are strongly intercorrelated, which can result in unstable and unreliable regression coefficient estimates. To detect the presence of multicollinearity, we utilized the variance inflation factor (VIF), which measures the extent to which the variance of a regression coefficient estimate increases owing to the correlation among predictor variables. A VIF value surpassing the cutoff point of 10 is commonly considered a strong indication of problematic multicollinearity [52]. To enhance the model interpretability and alleviate the consequences of multicollinearity, we removed variables with VIF values surpassing the threshold of 10 from further analyses. Moreover, we explored the possibility of interaction effects among the predictor variables, which arises when the level of a predictor variable influences the impact of another predictor variable on the response variable. To uncover potential interactions between features, we conducted a stratified analysis involving dividing the data into subgroups on the basis of the levels of a suspected interacting variable and assessing relationships between the predictor and response variables within each subgroup. Specifically, we investigated how image resolution might modulate the association between trichome density and nitrate concentration in tomato leaves.

3.4 Analysis of Tomato Fertilization Requirements Based on Leaf Trichome Density

3.4.1 Problem formulation and objectives

The primary objective of this study was to develop a kit that is suitable for practical use in the field. By leveraging existing knowledge on the correlation between leaf nitrogen-related indica-

tors, we aimed to address a crucial question for farmers, which is affected by the fertilizer stress level and trichome density: Do my tomato plants in the field require additional fertilization?

3.4.2 Model design and variable selection

Consequently, we formulated a binary classification problem to determine the need for fertilization on the basis of leaf nitrate ion concentrations. The threshold for the leaf nitrate ion concentration was set as a parameter. Importantly, there is no universally ideal level of fertilizer stress for tomatoes. This level can vary depending on the environmental conditions and specific goals of the cultivator. Recognizing this variability, our study did not set a specific nitrate ion threshold. Instead, we parameterized the threshold for the leaf nitrate ion concentration in our model. This threshold was used to determine whether additional fertilization was necessary: If the concentration exceeded the threshold, no additional fertilization was needed, whereas concentrations below the threshold indicated a need for fertilization. This binary decision was then used as the target variable in our model.

For the explanatory variables in this model, we used the NND, image resolution and exposure time. We applied standard scaling to these explanatory variables to ensure that all variables were on a comparable scale and to improve the model’s performance. This scaling technique transforms the variables so that their mean is zero and their standard deviation is one.

In our cross-validation process, the data were divided into training and test sets. Importantly, the primary focus of this research was to develop a kit suitable for practical field use, with an emphasis on architectural-level improvements. Specifically, a quantitative method for characterizing tomatoes and refinement of measurement methods were selected. Therefore, we did not employ hyperparameter tuning using a validation dataset. Instead, we used default values for the model’s hyperparameters. This decision may lead to underfitting or overfitting due to insufficient control over model complexity, potentially resulting in reduced generalization performance and missed opportunities for theoretical performance analysis and optimization [53]. However, we deemed these potential drawbacks acceptable, given that our primary objective was to prioritize the development of a practical and accessible kit for field use, rather than achieving the highest possible model performance.

3.4.3 Cross-validation strategy

To evaluate the model’s generalization performance, we employed leave-one-out cross-validation (LOOCV) for each compound leaf. This method was chosen because of the relatively small-scale dataset, derived from 40 compound leaves harvested from 20 tomato plants from the three intervention groups. These compound leaves yielded 300 leaflets, and we analyzed 6,855 images taken of these leaflets. Given this dataset structure, LOOCV was deemed suitable for minimizing bias from specific samples while maximizing the use of our limited but diverse data points. Furthermore, our feature extraction process enables learning with tabular data, maintaining low computational costs despite the iterative nature of LOOCV.

In each iteration of the LOOCV process, a single unique compound leaf was selected. The data derived from this selected compound leaf served as the test set, whereas the data from the remaining compound leaves constituted the training set.

3.4.4 Evaluation methodology

Because the kit users can easily and cost-effectively perform multiple measurements, we evaluated the model’s predictive performance via a method that averages multiple predictions obtained from multiple images into a single prediction. We randomly extracted 1 to 25 rows of data from the test set and input them into the model. This method simulates scenarios where users capture and utilize 1 to 25 images simultaneously for prediction, which allows us to assess

the model’s performance under various measurement intensities. This assessment enables us to understand how the model’s performance improves with an increasing number of measurements. To ensure a comprehensive evaluation, we aggregated the predictions and actual observations from all cross-validation iterations: This combined data is used to calculate various performance metrics.

3.4.5 Parameter range selection

To effectively visualize the analysis results, the range of nitrate ion concentrations and the number of images used for evaluation were narrowed to specific ranges or values. This refinement process was guided by practical considerations and domain knowledge.

With respect to the nitrate ion concentration threshold, setting a single universal value is inappropriate because of the variability in agricultural conditions. We could define a relevant range on the basis of domain knowledge. Two key factors influenced this decision. First, nonlinear models such as LightGBM, which we used for modeling, tend to produce unstable predictions near or outside the boundaries of the training data. Second, agricultural workers and related economic entities primarily sustain their livelihoods through crop production revenues. Consequently, it is crucial to avoid excessive fertilizer stress, which could lead to decreased profitability. Considering these points, we decided to exclude the low nitrate concentration region from the threshold setting. Such a scenario is unlikely to be used in a practical application of the kit.

As our kit allows for multiple measurements to be easily and cost-effectively performed, we set the upper limit for the number of images used in the evaluation to 25. This decision balances the need for comprehensive data with practical considerations of time and resource efficiency in real-world applications.

Based on these considerations, we defined our range of interest for nitrate ion concentrations from the second quartile to the third quartile of the distribution obtained from our experiments. For visualizations requiring specific parameter settings, we used the third quartile value as the nitrate ion concentration threshold and set the number of images for evaluation to 25. We refer to this combination of parameter settings as the "representative parameter setting". This approach allowed us to evaluate and visualize the model’s performance within a practical and statistically meaningful range. To ensure comprehensive reporting, performance evaluations using all the parameters, including those outside the defined range of interest, are presented in the appendix.

3.4.6 Data analysis workflow

Algorithm 6 presents a schematic overview of the data analysis workflow. The main processes of model training and evaluation are described in detail below.

3.4.7 Feature preprocessing and label setting

The objective of the modeling was to determine the need for additional fertilization by comparing the nitrate ion concentration, estimated from the trichome density in images, with a predefined threshold. Consequently, leaves were labeled 0 (indicating no need for additional fertilization) or 1 (indicating the need for additional fertilization) based on whether the nitrate ion concentration was below or above the threshold, respectively.

3.4.8 Model training

The dataset was partitioned into training and testing sets before the modeling process. The modeling task involved binary classification, with the data being divided based on each compound leaf. To address the imbalance in both the number of images between compound leaves and leaflets and the class labels, the minority class was oversampled via the synthetic minority oversampling technique (SMOTE)[54, 55].

Algorithm 6 Tomato fertilization requirement prediction

Require: X : Explanatory and moderator variables

Require: Y : Target variables

Require: t : Threshold for nitrate ion concentration

Require: n : Measurement intensity

Require: M : Metadata containing CompoundLeafIndex etc.

Ensure: $metrics$: Performance metrics

Ensure: S : SHAP values

```
1: function SETLABELS( $Y, t, M$ )
2:    $L \leftarrow \emptyset$ 
3:   for  $i \leftarrow 1$  to  $|Y|$  do
4:      $label \leftarrow Y[i] < t?0 : 1$ 
5:      $M[i]['ClassLabelIndex'] \leftarrow label$ 
6:      $L \leftarrow L \cup \{label\}$ 
7:   end for
8:   return  $M, L$ 
9: end function
10: function APPLYSMOTE( $X, Y, M$ )
11:   Apply SMOTE to  $X$  and  $Y$  based on  $M$ 
12:   return balanced  $X, Y$ 
13: end function
14: function TRAINMODEL( $X, Y$ )
15:   Train model on  $X, Y$ 
16:    $Y_{pred} \leftarrow \text{MAKEPREDICTIONS}(model, X)$ 
17:   return  $Y, Y_{pred}, model$ 
18: end function
19: function EVALUATE( $model, X, Y, n, M_{test}$ )
20:   MakePrediction
21:   return  $Y, Y_{pred}$ 
22: end function
```

Main Execution

```
23:  $M, L \leftarrow \text{SETLABELS}(Y, t, M)$ 
24:  $Y_{train\_true}, Y_{train\_pred}, Y_{test\_true}, Y_{test\_pred} \leftarrow \emptyset$ 
25:  $S \leftarrow \emptyset$ 
26:  $I \leftarrow \text{EXTRACTCOMPOUNDLEAFINDEX}(M)$ 
27: for each unique index  $i$  in  $I$  do
28:    $X_{test} \leftarrow$  Select rows from  $X$  where  $I$  equals  $i$ 
29:    $Y_{test} \leftarrow$  Select rows from  $Y$  where  $I$  equals  $i$ 
30:    $M_{test} \leftarrow$  Select rows from  $M$  where  $I$  equals  $i$ 
31:    $X_{train} \leftarrow$  All rows from  $X$  except where  $I$  equals  $i$ 
32:    $Y_{train} \leftarrow$  All rows from  $Y$  except where  $I$  equals  $i$ 
33:    $M_{train} \leftarrow$  All rows from  $M$  except where  $I$  equals  $i$ 
34:    $X_{train}, Y_{train} \leftarrow \text{APPLYSMOTE}(X_{train}, Y_{train}, M_{train})$ 
35:    $Y_{true}, Y_{pred}, model \leftarrow \text{TRAINMODEL}(X_{train}, Y_{train})$ 
36:    $Y_{train\_true} \leftarrow Y_{train\_true} \cup Y_{true}$ 
37:    $Y_{train\_pred} \leftarrow Y_{train\_pred} \cup Y_{pred}$ 
38:    $Y_{test}, Y_{pred} \leftarrow \text{EVALUATE}(model, X_{test}, Y_{test}, n, M_{test})$ 
39:    $Y_{test\_true} \leftarrow Y_{test\_true} \cup Y_{test}$ 
40:    $Y_{test\_pred} \leftarrow Y_{test\_pred} \cup Y_{pred}$ 
41:    $S \leftarrow S \cup \text{COMPUTESHAP}$ 
42: end for
43:  $metrics \leftarrow \text{CALCULATEMETRICS}$ 
```

Modeling was performed via a light gradient boosting machine (LightGBM), a decision tree-based approach that employs gradient boosting techniques to combine multiple decision trees for learning purposes [54]. In LightGBM, each decision tree uses the residuals from the previous tree to improve the overall predictive accuracy of the model iteratively. The regression predictions z were calculated via Equation 4 [56].

$$z = \sum_{k=1}^K f_k(x) \quad (4)$$

In Equation (4), $f_k(x)$ is defined as the output generated by the k -th decision tree. Here, k represents the total number of decision trees, and x corresponds to the input feature vector. The regression prediction z is then passed through the sigmoid function, as shown in Equation 5, to calculate the probability \hat{y} .

$$\hat{y} = \frac{1}{1 + e^{-z}} \quad (5)$$

The sigmoid function in Equation (5) maps the value of z to a probability between 0 and 1, which is then interpreted as the likelihood of the input belonging to class 1. By applying the sigmoid function to the regression predictions z , as shown in Equation (5), we simulate a scenario in which farmers are provided with the predicted probabilities of nutrient deficiency, enabling them to make informed decisions about the application of additional fertilization to their fields. The final class label \hat{Y} was determined based on the computed probability \hat{y} , according to the decision rule outlined in Equation 6.

$$\hat{Y} = \begin{cases} 1 & \text{if } \hat{y} \geq 0.5 \\ 0 & \text{if } \hat{y} < 0.5 \end{cases} \quad (6)$$

To train the classification model, the default parameters of the LightGBM library were employed, including a learning rate of 0.1 and 100 boosting rounds.

3.4.9 Model evaluation and feature importance

The predicted labels \hat{Y} were compared to the true labels, and performance metrics were computed. The evaluation metric used during training was the area under the precision-recall curve (AUC-PR), as defined by Equation 11. To evaluate the performance of the trained model on the test data, several evaluation metrics were employed, including the precision, recall, F_1 , area under the receiver operating characteristic curve (AUC-ROC), AUC-PR, and mean AUC-PR (mPR). These metrics are described by Equations 7-12.

The precision, as defined by Equation 7, is the ratio of correctly predicted positive observations to the total number of predicted positives [57, 58].

$$\text{Precision} = \frac{\text{True Positive}}{\text{True Positive} + \text{False Positive}} \quad (7)$$

Equation 8 defines recall as the proportion of accurately predicted positive observations in relation to the total number of true positives. This metric evaluates the model's ability to identify all relevant positive instances.

$$\text{Recall} = \frac{\text{True Positive}}{\text{True Positive} + \text{False Negative}} \quad (8)$$

Equation 9 represents the F_1 score, which is calculated as the harmonic mean of the precision and recall. This metric serves as a balanced measure of both metrics.

$$F_1 \text{ Score} = \frac{\text{Precision} \times \text{Recall}}{\text{Precision} + \text{Recall}} \quad (9)$$

Equation 10 represents the AUC-ROC, which is the area under the curve of the true positive rate versus the false positive rate. $t(f)$ denotes the true positive rate at a given false positive rate f . This measure effectively summarizes the model’s ability to discriminate between the positive and negative classes across all possible thresholds, providing a single scalar value that reflects the trade-off between sensitivity (true positive rate) and specificity ($1 - \text{false} - \text{positiverate}$).

$$\text{AUC-ROC} = \int_0^1 t(f)df \quad (10)$$

Equation 11 represents the AUC-PR, which defines the area under the precision versus recall curve. $p(r)$ represents the precision at a given recall value r . This metric provides a single scalar value that summarizes the trade-off between precision and recall across all possible thresholds. The AUC-PR is particularly useful for datasets with imbalanced class distributions, as it provides a more informative measure than does the AUC-ROC [58].

$$\text{AUC-PR} = \int_0^1 p(r)dr \quad (11)$$

Equation 12 provides a definition for the mROC, which quantifies the AUC-ROC for various thresholds k of the nitrate ion concentration. To provide a more precise evaluation, the algorithm calculates the average AUC-ROC value within the specified threshold range of 1600-1900 parts per million (ppm) of the nitrate ion concentration. The establishment of this threshold range is based on the concentrations of nitrate ions observed in tomato leaves that have demonstrated favorable yields. In the agricultural domain, it is impractical to consider a situation where a model incorporating a threshold resulting in a decrease in crop productivity would be employed. For each threshold k , the cumulative AUC-ROC_k is divided by the total number of models m . Within this framework, the AUC-ROC_k represents the area under the precision-recall curve for a specific threshold k , whereas m denotes the total number of models considered. The mROC is used to assess the model’s performance across a wide range of threshold values, evaluating its effectiveness in various operational scenarios.

$$\text{mROC} = \frac{1}{m} \sum_{k=1600}^{1900} \text{AUC-ROC}_k \quad (12)$$

Similarly, equation 12 defines mPR, which quantifies the average AUC-PR across the same threshold range (1600-1900 ppm) of nitrate ion concentration. AUC-PR_k represents the area under the receiver operating characteristic curve for a specific threshold k . The mROC provides an alternative metric to assess the model’s discrimination ability across different threshold values, complementing the evaluation based on mPR. To gain insights into the contribution of each feature to the model’s predictions, we employed Shapley additive explanations (SHAP) values [59].

$$\text{mPR} = \frac{1}{m} \sum_{k=1600}^{1900} \text{AUC-PR}_k \quad (13)$$

3.5 Analysis of Trichome Density in Relation to Fertilizer Stress

3.5.1 Research objectives and scope

The primary objective of this research is to develop practical tools for farmers to address agricultural challenges. Specifically, fertilizer stress in tomato plants has been assessed. This assessment is achieved through reverse inference, utilizing a known natural phenomenon: the change in leaf trichome density in response to variations in fertilizer stress. This approach allows us to infer fertilizer stress levels on the basis of observed trichome density patterns. Although our experimental design is optimized for this applied goal, it also provides an opportunity to contribute,

albeit secondarily, to the scientific understanding of the relationship between fertilizer stress and trichome density in tomato plants as a natural phenomenon.

3.5.2 Quantitative analysis approach

Leveraging this opportunity, we employed a machine learning approach with a regression model to investigate the quantitative relationship between fertilizer stress and trichome density in tomato plants. This analysis served as a forward inference step, establishing a predictive model for trichome density based on three features: nitrate ion concentration and two moderator variables of image acquisition: image resolution and exposure time.

3.5.3 Model selection and configuration

We implemented the LightGBM algorithm for our regression model, using default hyperparameters. Specifically, the model was configured with an L2 loss objective function, 100 boosting rounds, and a learning rate of 0.1.

3.5.4 Cross-validation and data preprocessing

To rigorously assess the model’s performance and generalizability, we implemented a LOOCV strategy. This approach involved iteratively using each unique leaflet as a test set, while the remaining data served as the training set.

Prior to model training, we applied standard scaling to the feature variables and the target variable. For each LOOCV fold, we trained a LightGBM model on the scaled training data and used it to predict the NND for the test set. The predictions were then inverse-transformed to the original scale for evaluation.

We assessed the model’s performance via several metrics, including the root mean square error ($RMSE$), Coefficient of determination (R_2) and the Pearson correlation coefficient (R).

4 Results

4.1 Nitrate Ion Concentrations in Compound Leaves as Lagging Indicators of Fertilizer Stress

Figure 10 shows the distribution of nitrate ion concentrations in compound leaves located 15 cm from the apical meristem, measured across experimental plots subjected to three different fertilizer concentrations: high, intermediate, and low. Notably, higher fertilizer application rates corresponded to elevated nitrate ion concentrations within the compound leaves.

Statistical analysis via the Kruskal-Wallis test yielded a p value < 0.05 , indicating significant differences among the three groups. Subsequent pairwise comparisons via the Mann-Whitney U test, adjusted for multiple comparisons via the Bonferroni correction, revealed statistically significant differences between the high-low and intermediate-low groups (adjusted $p < 0.05$). However, no statistically significant difference was observed between the high-intermediate subgroup (adjusted $p = 0.52$). This lack of a significant difference between the high- and intermediate-level fertilizer treatments may reflect the trend of diminishing returns. These findings suggest that the maximum yield is greater in the high-intensity fertilizer treatment than in the low-intensity treatment, beyond which additional fertilizer inputs provide increasingly smaller yield gains.

These results suggest that the compound leaf nitrate ion concentration can serve as a reliable indicator of fertilizer stress in tomatoes, particularly for distinguishing between low and high fertilizer levels. However, it is important to acknowledge the variability observed in the relationship between nitrate ion concentration and fertilizer level. The overlapping distributions and nonsignificant differences between the high- and intermediate-level fertilizer treatments are

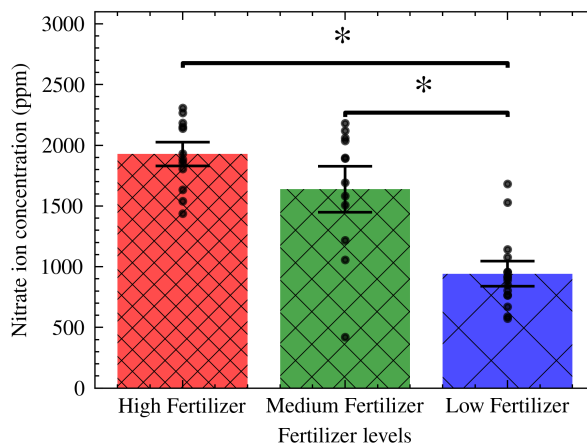


Figure 10: **Distribution of nitrate concentrations in compound leaves at different fertilizer levels.**

shown in Figure 10. This variability underscores the importance of directly assessing plant nitrate uptake rather than relying solely on fertilizer application rates to accurately evaluate fertilizer stress. Directly measuring plant nutrient uptake can provide a more comprehensive understanding of nutrient availability, accounting for factors beyond fertilizer application that may influence nutrient absorption.

4.2 Leaf Nitrate Concentration as a Leading Indicator of Fruit Yield

Figure 11 shows a positive correlation between fruit yield and nitrate concentration in compound leaves. This finding indicates that the nitrate ion concentration in compound leaves can serve as an indicator of fruit yield. Generally, crop yield tends to increase with increased fertilizer absorption; however, fertilizer application beyond a certain threshold can reduce yields [4, 8, 9]. The findings of this study indicate that fertilizer application in the experimental field fell below this critical threshold. These findings suggest that the tomatoes experienced stress due to insufficient fertilization.

As detailed in the Parameter Range Selection section, various factors were considered when determining an appropriate nitrate concentration threshold for visualization purposes. Based on these considerations, we employed the third quartile value of 1,783 ppm, derived from the measured leaf nitrate concentrations, to illustrate the model’s performance in distinguishing between different yield potentials.

Figure 12 presents the cumulative yield of the experimental setup, calculated as the weighted average of individual intervention trial plots within the experimental environment. The final fruit production capacity of the experimental apparatus was determined to be 39.12 kg m^{-2} on the basis of the planting density. This value aligns favorably with commercial tomato yields reported in previous studies [60], indicating that the environmental conditions within the experimental setup, which comprehensively encompass crucial factors for plant growth, such as temperature, humidity, light, water availability, oxygen levels, and carbon dioxide concentrations, effectively simulated those of commercial tomato production.

4.3 Handling of Multicollinearity and Variable Interaction in Data Analysis

The statistical model necessitates the exclusion of ISO speed ratings as a variable because of the manifestation of multicollinearity. A Farrar-Glauber test was conducted to assess multicollinearity, revealing a significant presence ($p < 0.001$) [61]. This result indicates a statistically significant linear dependence among the explanatory variables. Table 4 presents the variance

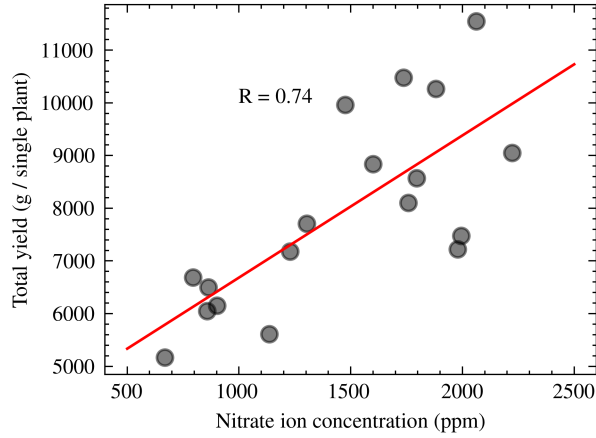


Figure 11: **Relationship between the nitrate ion concentration in compound leaves and yield.**

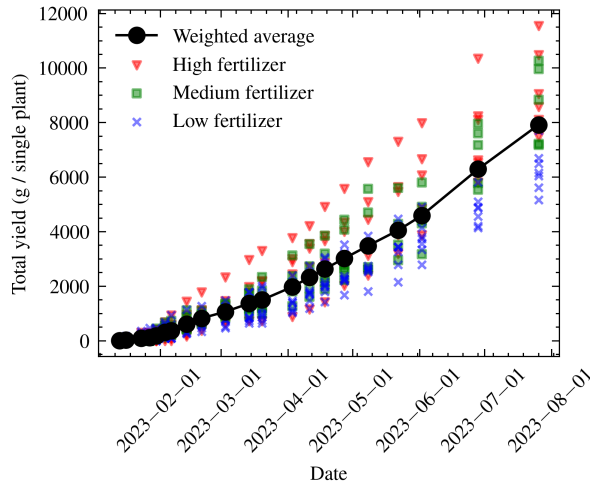


Figure 12: **Cumulative fruit yield in the experimental setup.**

Table 4: Examination of Multicollinearity through the VIF

Feature	VIF
Nearest Neighbor Distance	43.60
Resolution	11.03
Exposure Time	4.98
ISO Speed Ratings	47.80

inflation factor (VIF) for each variable. Notably, the ISO speed ratings exhibit an exceptionally high VIF of 47.80, substantially exceeding the conventional threshold of 10 and thus confirming severe multicollinearity.

The ISO speed ratings may inadvertently function as a mediating variable between trichome density and fertilizer stress, attributable to the camera’s automatic exposure (AE) function. The AE system responds to the overall image brightness. This phenomenon is considerably influenced by trichomes appearing as white points due to the reflection of light from the LED of the smartphone. Variations in trichome density, induced by fertilizer stress, alter image

Table 5: Interaction when Stratified Based on Resolution

Percentile	Resolution (pixel)	Equation
Higher than 85th	$> 1.08 \times 10^6$	$y = 3.06 \times 10^{-2}x + 170$
15th to 85th	$1.08 \times 10^6 - 5.56 \times 10^5$	$y = 1.90 \times 10^{-2}x + 205$
Lower than 15th	$< 5.56 \times 10^5$	$y = 1.28 \times 10^{-2}x + 254$

brightness, prompting automatic adjustments in ISO sensitivity. Consequently, the ISO speed rating becomes an indirect indicator of trichome density and, by extension, fertilizer stress.

This intricate relationship positions ISO sensitivity as a mediator variable, not through direct measurement of trichomes or fertilizer stress but by reflecting the camera’s response to image characteristics indicative of these factors. The high VIF value for ISO speed ratings can be attributed to this complex interaction, where the camera’s real-time exposure adjustment algorithm effectively renders ISO sensitivity dependent on trichome density, which is, in turn, influenced by fertilizer stress. This unintended mediation effect introduces complications into the dataset: ISO sensitivity becomes correlated with the variable of interest (trichome density) and the target variable (fertilizer stress).

Notably, although multicollinearity may not significantly affect the overall predictive performance of the model as evaluated by cross-validation, it can substantially impact the interpretation of individual variable importance. In the presence of multicollinearity, estimated coefficients for individual predictors may become unstable and unreliable. This instability can lead to biased assessments of variable importance, potentially resulting in overestimation or underestimation of the importance of certain variables in the model.

In the context of this study, where both the generalization performance and model interpretability through cross-validation are paramount, it is imperative to exclude the ISO speed ratings as a variable because of their demonstrated multicollinearity. This exclusion enhances the robustness and interpretability of the statistical model, ensuring more reliable insights into the relationships between trichome density, fertilizer stress, and other relevant variables.

The resolution value exhibits interactions and a shift in the intercept, necessitating its inclusion as a variable within the statistical model. An investigation of the effect of resolution on the relationship between trichome density and nitrate concentration in compound leaves reveals varying coefficients and intercepts in the regression equation. These changes in the coefficients with respect to the resolution are demonstrated in Table 5 and Figure 13. The resolution inherently varies because of factors such as camera performance and the distance between the camera sensor and the measurement paper. Consequently, in the dataset used in this study, the resolution is an indicator of the distance between the camera and the measurement paper. Thus, to avoid omitted variable bias, which could lead to misinterpretation of the effects of one variable as those of another, it is crucial to include resolution as a variable in the model. Furthermore, the varying coefficients demonstrate the advantages of using higher-resolution images for trichome detection in computer vision applications. The results show that increased resolution leads to improved detection accuracy, highlighting the importance of holding the measurement paper close to the camera and using a high-resolution image sensor for such tasks.

Table 6 displays the VIF values for all the variables except for the ISO speed ratings. After excluding ISO speed ratings, no variables with a VIF exceeding 10 were identified, indicating that multicollinearity was no longer a concern. To improve the interpretability of the model, ISO speed ratings were excluded as a variable in subsequent analyses because of their strong correlation with other variables and their potential to obscure the individual effects of each predictor. Instead, the modeling process included variables such as NND, resolution, and exposure time, which were deemed to have a more independent impact on the response variable.

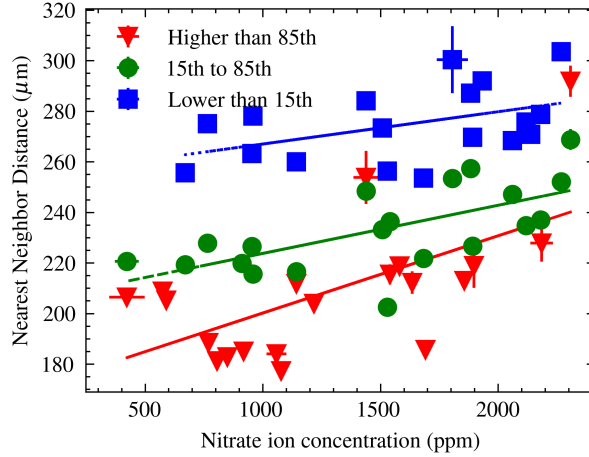


Figure 13: Effect of resolution on the relationship between trichome density and nitrate concentration in leaves.

Table 6: VIF Value after Dimensionality Reduction

Feature	VIF
Nearest Neighbor Distance	8.63
Resolution	6.49
Exposure Time	3.10

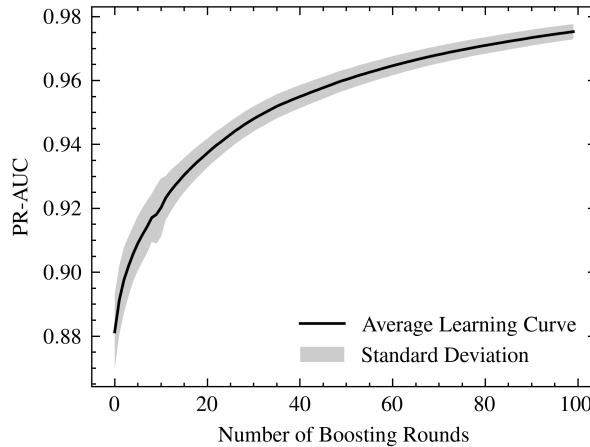


Figure 14: Learning curve of the LightGBM model.

4.4 Performance of the Proposed Method

Figure 14 shows the learning curve of the LightGBM model over 100 boosting rounds with default settings. A gradual increase is observed in the AUC-PR values for the training sets after each boosting round. This improvement indicates that the model has been adequately trained.

Table 7 shows the predictive performance of the classification model at the different nitrate concentration thresholds. With respect to the trade-off between precision and recall, the model achieves highly balanced values.

For subsequent analyses, we defined a representative scenario using a nitrate concentration threshold of 1,783 ppm and 25 images captured from a single compound leaf. Using this representative scenario, predictions were made, allowing for an accurate assessment of the need

Table 7: Predictive Performance in Terms of the Need for Additional Fertilizer using LOOCV at Various Nitrate Ion (ppm) Thresholds when Using the 25 Image Features

Evaluation Metrics	1600	1750	1900
Precision	0.68	0.76	0.79
Recall	0.66	0.76	0.79
F1 Score	0.67	0.76	0.79
PR AUC	0.76	0.84	0.87
ROC AUC	0.64	0.68	0.58

Table 8: Comparison of Predictive Performance between the Proposed Model and the Baseline Model in a Representative Parameter Setting

Model	Precision	Recall	F1 Score	ROC AUC	PR AUC
Proposed	0.79	0.78	0.79	0.81	0.87
Baseline	0.62	0.49	0.55	0.50	0.72

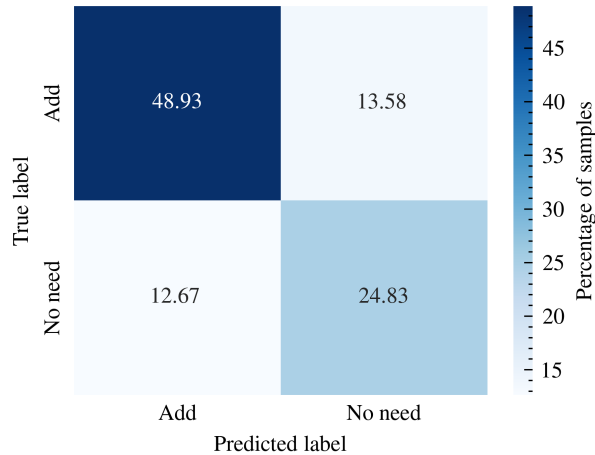


Figure 15: Confusion matrix for classification outcomes during LOOCV in a representative parameter setting.

for additional fertilization. The predictive performance, as evaluated by the mROC, is 0.64, and, as evaluated by the mPR, it is 0.82 despite variations in the measurement data caused by differences in optical conditions.

Figure 15 shows a confusion matrix depicting true positives, false positives, true negatives, and false negatives. The predictions do not show substantial bias toward false positives or false negatives, indicating a balanced performance in identifying both classes correctly. This lack of bias is also evident from the balanced results presented in Table 7, which includes the F1 score and AUC-PR and AUC-ROC values, as well as the PR curve in Figure 16 and the ROC curve in Figure 17.

Table 8 compares the performance of the proposed model and the baseline model. The baseline model uses a simple majority class predictor. This comparison utilizes the metrics defined in Equations 7-11, using the representative parameter setting. The table demonstrates the improved performance of the proposed model across all evaluated metrics.

Figure 18 illustrates the relationship between the number of input images and the model's

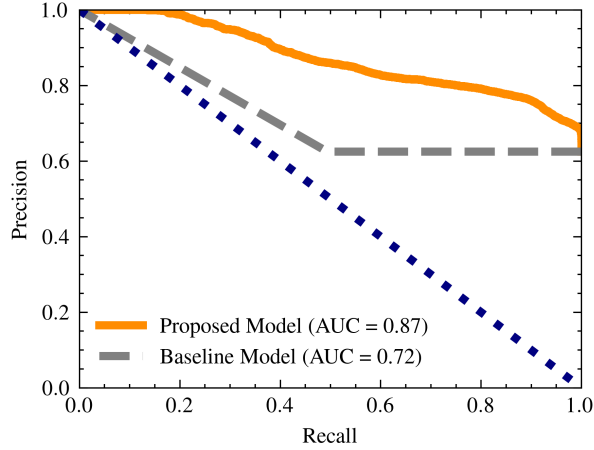


Figure 16: Precision-recall (PR) curve analysis of the model during LOOCV in a representative parameter setting.

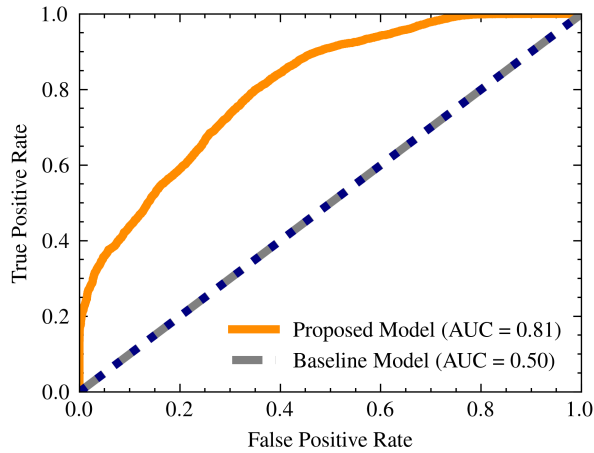


Figure 17: Receiver operating characteristic (ROC) curve analysis of the model during LOOCV in a representative parameter setting.

predictive performance. Using a single image yields a mean AUC-PR (mPR) of 0.80, and increasing the number of input images leads to better predictive performance.

Figure 19 illustrates the global feature contributions based on SHAP values, providing insights into the overall model interpretation. NND has a high mean absolute SHAP value, suggesting its significant contribution to the model’s predictions across the dataset.

4.5 Effect of Fertilizer on Trichome Density

To quantitatively evaluate the relationship between trichome density on tomato leaves and nitrogen nutritional status, we conducted modeling via NND. Figure 20 presents the results of an NND prediction model employing nitrate ion concentration, image resolution, and exposure time as explanatory variables. The coefficient of determination (R^2) for this model is 0.63, indicating that the combination of explanatory variables (nitrate ion concentration) and moderating variables (image resolution, exposure time) can account for approximately 62.48% of the variation in trichome density (represented by NND) of leaflets obtained from fertilizer intervention experiments.

Notably, this study was designed primarily to focus on the development of image-processing technology rather than being a rigorous hypothesis-testing study for interpreting natural phe-

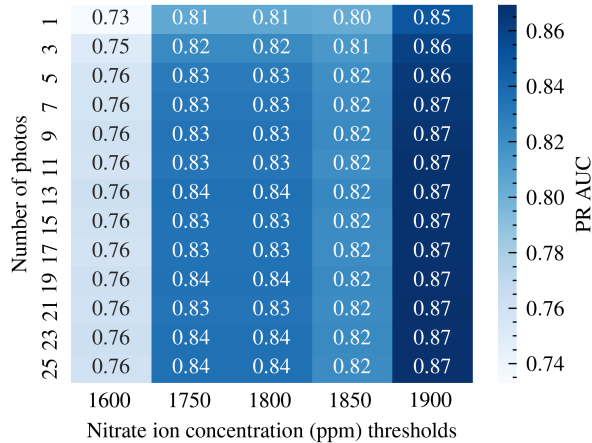


Figure 18: **Model prediction performance when various thresholds and numbers of images are set.**

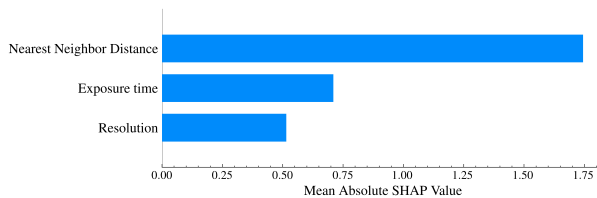


Figure 19: **Feature contribution during LOOCV with a representative model setting.**

nomena in complex system. Typically, a hypothesis-based approach starts with a specific hypothesis or theory, and experiments are designed to test the validity of this hypothesis in a deductive manner [62]. In contrast, while a simple hypothesis existed for conducting experimental work as shown in Figure 3, this study primarily adopted a data-driven approach, where hypotheses and models are generated inductively based on patterns and relationships found within the dataset.

Therefore, it is appropriate to interpret the results of this study as an analysis stemming from a data-driven approach. However, the relationship between trichome density on tomato leaves and nitrogen nutritional status has been quantitatively verified in previous studies through hypothesis-based research [24]. As this study aims to capture general trends rather than subtle differences, the need for strict hypothesis-based experimentation is relatively low. Consequently, by adopting an inductive research method, the likelihood of fatal bias is considered low, and the data-driven approach of this study supports the possibility that fertilizer stress may affect trichome density, particularly in young leaves.

Nevertheless, the existence of unexplained variation (approximately 37.52%) in the model suggests the need for further investigation of additional factors and model improvements in future research.

5 Discussion

Tomatoes pose a challenge for detecting fertilizer stress through noncontact optical measurements of young leaf chlorophyll. This challenge arises from the nonlinear relationship between optical measurements and leaf nitrogen content, which distinguishes tomatoes from other crops [7, 18]. To address this problem, our study focused on trichomes, which are densely packed hair-like structures on leaf surfaces that have been less explored in previous research. We investigated the feasibility of detecting fertilizer stress by developing a device that utilizes trichome

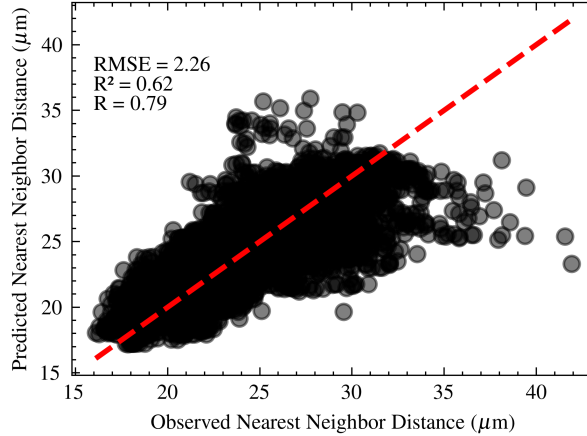


Figure 20: **Modeling of NND using nitrate concentration, resolution, and exposure time.**

density as a primary predictor. Our findings suggest the possibility of overcoming the limitations of conventional noncontact optical methods in assessing tomato fertilizer conditions. Our approach opens new avenues for developing diagnostic devices that consider leaf surface structure. However, the diagnostic kits developed in this study have some limitations regarding their performance. We validated the performance of the kit through experiments using a well-designed setup that simulated different levels of fertilizer stress commonly found in agricultural production conditions. In addition, the tomato cultivation method used in the present study involved cost-effective hydroponic cultivation via plastic buckets. The yields achieved were comparable to those obtained in commercial cultivation. This finding suggests that the cultivation method employed in this study closely simulated agricultural production conditions. However, it is uncertain whether all farmers will be able to establish optimal growing conditions for tomatoes to achieve higher yields, considering the financial costs involved in acquiring the necessary equipment. Consequently, environmental stresses beyond fertilizer stress could be encountered, which could decrease the predictive performance of our novel method under these circumstances.

Traditionally, farmers have relied on visual inspection of leaf color, size, texture and overall plant health to assess the nutrient status of plants. However, the accuracy of this method highly depends on the farmers' experience and motivation, resulting in considerable variations among individuals. Consequently, standardizing the assessment of nutrient status becomes problematic, making it difficult to compare and evaluate the effectiveness of different approaches. The absence of standardization in nutrient status assessment hinders highly advanced evaluation of the usefulness of diagnostic kits for a certain farmer solely on the basis of a comparison of their predictive accuracy. Thus, further demonstrations and validations employing more lagging indicators, such as financial metrics, are necessary to assess the practical applicability of these diagnostic kits in real-world agricultural settings.

Although various nutrient diagnostic kits are commercially available for assessing plant nutrient status, their high cost and potential difficulties in application to delicate plant tissues, such as young tomato leaves, limit their widespread adoption in practical farming settings. To overcome these challenges, we propose a novel, simple, and cost-effective method for assessing nutrient status in tomato plants, with a specific focus on young leaves, which are typically relatively sensitive to nutrient deficiencies and play a crucial role in plant growth and development.

In addition to tomatoes, various plant species, including agriculturally important crops such as watermelon (*Citrullus lanatus*), egg plants (*Solanum melongena*), tobacco (*Nicotiana tabacum*), soybean (*Glycine max*), and cannabis (*Cannabis sativa*), are known to have abundant trichomes. The proposed trichome-based method for assessing nutrient status has application potential in other plant species with dense trichomes near their growing points, expanding its

scope and potentially improving real-time nutrient management practices in a wide range of crops, thereby enhancing the efficiency and precision of fertilizer application. By optimizing fertilizer application and reducing waste, this method could lead to increased crop yields, lower production costs, and reduced environmental impact, ultimately contributing to more sustainable agricultural practices. Further research is needed to validate the effectiveness of this method in various crop species and investigate the potential integration of this approach with other precision agriculture technologies, such as remote sensing, for more comprehensive and efficient nutrient management strategies.

6 Conclusions

This study focused on developing a novel method for detecting fertilizer stress in tomato plants by measuring the density of trichomes on their leaves. The study also included setting up and evaluating the experimental environment necessary for conducting these assessments. The developed diagnostic kit enables noninvasive and early detection of fertilizer stress in plants, obviating the need for customized sensing device design and permitting the use of a universal diagnostic kit at a lower cost than traditional devices while accurately assessing the nutrient status of tomato plants. The findings of this study present a novel approach to designing diagnostic devices for detecting fertilizer stress in plants by considering the structure of the plant surface.

Appendix

A Simulation Demonstrating the Robustness of the Nearest Neighbor Distance

This appendix presents a simulation demonstrating the robustness of the nearest neighbor distance (NND) as a density metric compared with the conventional point count per unit area.

The simulation involves generating a set of points within a defined area. Damage is simulated by removing a portion of these points and then comparing the changes in the NND and the point count. To mimic the random spatial distribution of trichomes on a leaf surface, we employed a Poisson point process for point generation. The Poisson process is often used to model random events occurring independently in a given space or time, making it suitable for simulating the distribution of trichomes, which are expected to emerge randomly on the leaf surface.

The detailed steps are outlined in Algorithm 7.

Figure 21 shows an example of the point distribution before and after simulated damage. The points were randomly generated via a Poisson process within a 1000×1000 area. The damage was simulated by removing points within the right half of the area, as indicated by the "damage boundary" line. Figure 22 shows the histograms of NNDs before and after simulated damage.

The simulation results demonstrate that NND is more robust to point removal than the conventional density metric based on the point count per unit area. Figure 23 compares the NND and point count before and after simulated damage. Although both metrics decreased after damage, the decrease in NND was smaller than that in the point count.

To statistically validate this observation, we performed a Wilcoxon signed-rank test to compare the absolute change rates of the NND and the point count after damage, as shown in Figure 24. The test revealed a statistically significant difference between the two metrics ($p < 0.001$), supporting the hypothesis that NND is less affected by localized point loss than the point count per unit area is. This finding highlights the advantage of using NND as a density metric in scenarios where localized point loss might occur, such as trichome detachment from leaf surfaces.

Algorithm 7 Trichome distribution simulation

Require: λ : Expected number of events (trichomes)

Require: A : Total area of the region

Require: S : Random seed value

Ensure: P : Set of points representing trichome locations

Ensure: P' : Set of points after simulated damage

1: **function** SETSEED(S)

 Set a random seed to S

2: **end function**

3: **function** POISSONRANDOM(λ)

 Generate random numbers from the Poisson distribution **return** number of points

4: **end function**

5: **function** UNIFORMRANDOM(a, b)

 Generate random numbers from a uniform distribution **return** random number between a and b

6: **end function**

7: **function** GENERATEPOINTS(N)

 Generate N random points in the area **return** set of points P

8: **end function**

9: **function** SIMULATEDAMAGE(P)

 Remove points with $x > 500$ **return** set of remaining points P'

10: **end function**

Main Execution

11: SETSEED(S)

12: $N \leftarrow$ POISSONRANDOM(λ)

13: $P \leftarrow$ GENERATEPOINTS(N)

14: $P' \leftarrow$ SIMULATEDAMAGE(P)

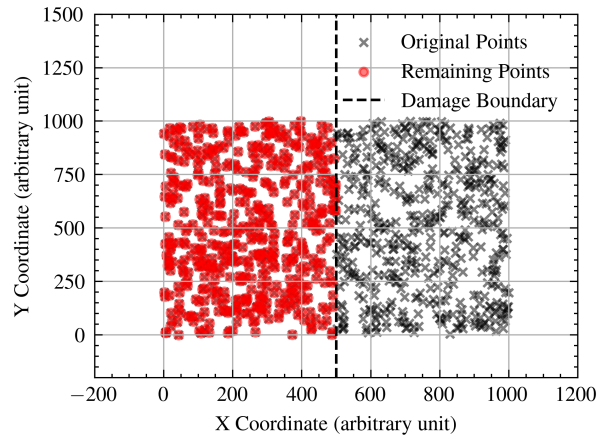


Figure 21: Point distribution before and after simulated damage.

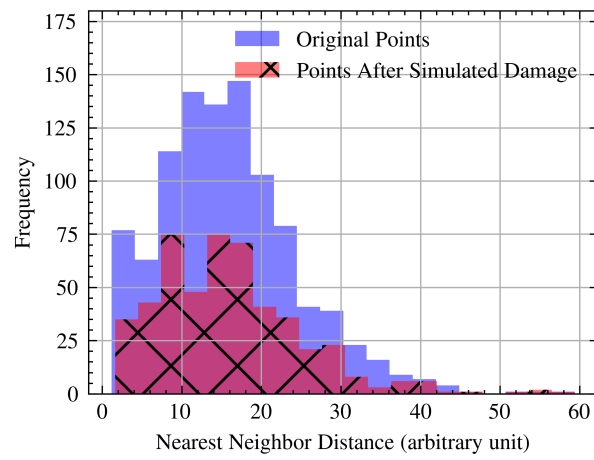


Figure 22: Histogram of nearest neighbor distances.

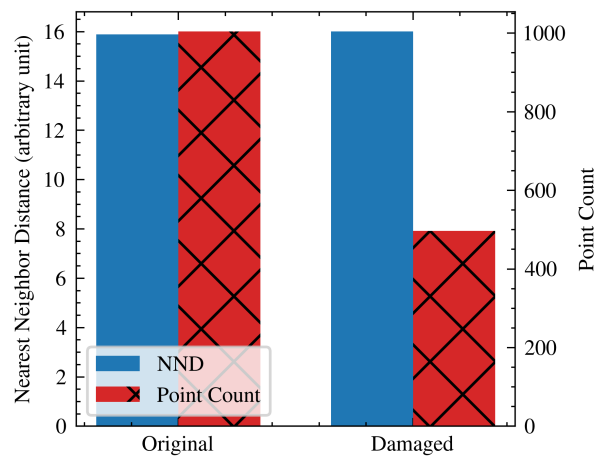


Figure 23: Comparison of NND and point count after simulated damage.

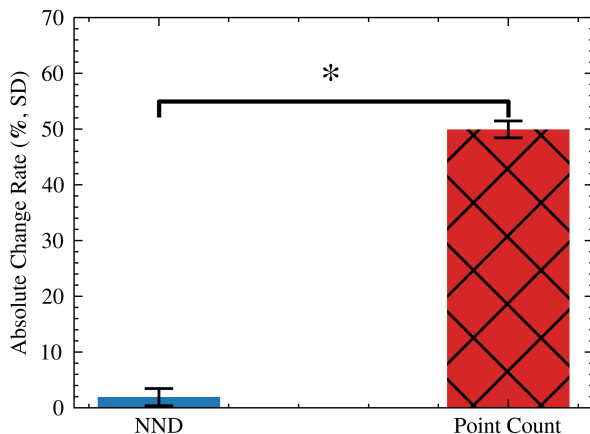


Figure 24: Comparison of NND and point count absolute change rates after simulated damage.

Table 9: Predictive Performance Comparison between Proposed and Baseline Models using LOOCV at Various Nitrate Ion Concentration Thresholds

Threshold	Precision	Recall	F1 Score	PR AUC	ROC AUC
600	0.15 (0.08)	0.04 (0.49)	0.06 (0.13)	0.13 (0.30)	0.51 (0.50)
777	0.12 (0.15)	0.11 (0.49)	0.11 (0.23)	0.18 (0.36)	0.48 (0.50)
955	0.39 (0.30)	0.42 (0.49)	0.40 (0.37)	0.49 (0.47)	0.57 (0.50)
1133	0.60 (0.38)	0.66 (0.49)	0.63 (0.43)	0.69 (0.53)	0.70 (0.50)
1311	0.61 (0.42)	0.66 (0.49)	0.63 (0.46)	0.71 (0.57)	0.67 (0.50)
1488	0.61 (0.45)	0.61 (0.49)	0.61 (0.47)	0.70 (0.59)	0.65 (0.50)
1666	0.71 (0.57)	0.68 (0.49)	0.69 (0.53)	0.79 (0.68)	0.65 (0.50)
1844	0.74 (0.78)	0.72 (0.49)	0.73 (0.60)	0.82 (0.83)	0.63 (0.50)
2200	0.95 (0.95)	1.00 (0.49)	0.97 (0.65)	0.97 (0.96)	0.50 (0.50)

B Comprehensive Model Performance across All Nitrate Ion Concentration Thresholds

Although Table 7 in the main text focused on the nitrate ion concentration range of 1600-1900 ppm, this section provides a more comprehensive evaluation of the model’s performance across the entire range of nitrate ion concentrations observed in our study. Table 9 presents the detailed results for the proposed and baseline models.

For this comprehensive analysis, we divided the full range of observed nitrate ion concentrations into 10 equal intervals: Each interval serves as a threshold for model evaluation. This approach allows for a thorough assessment of model performance across all possible thresholds within our dataset.

Table 9 illustrates the predictive performance of the proposed and baseline models using LOOCV at these various nitrate ion concentration thresholds. Both models utilized features extracted from 25 images per compound leaf. For clarity, the table presents the results for the proposed model as the main values, with the corresponding results for the baseline model shown in parentheses below.

References

- [1] C Sonneveld, J Van den Ende, and SS De Bes. “Estimating the chemical compositions of soil solutions by obtaining saturation extracts or specific 1:2 by volume extracts”. In: *Plant and Soil* 122 (Mar. 1990), pp. 169–175. DOI: 10.1007/BF02851971.
- [2] Yutiao Chen et al. “Crop management based on multi-split topdressing enhances grain yield and nitrogen use efficiency in irrigated rice in China”. In: *Field Crops Research* 184 (Dec. 2015), pp. 50–57. DOI: 10.1016/j.fcr.2015.09.006.
- [3] GJ Hochmuth. “Efficiency ranges for nitrate-nitrogen and potassium for vegetable petiole sap quick tests”. In: *HortTechnology* 4 (July 1994), pp. 218–222. DOI: 10.21273/HORTTECH.4.3.218.
- [4] Peter C Andersen et al. “Relationships of nitrogenous compounds in petiole sap of tomato to nitrogen fertilization and the value of these compounds as a predictor of yield”. In: *HortScience* 34 (Apr. 1999), pp. 254–258. DOI: 10.21273/HORTSCI.34.2.254.
- [5] Betty Klepper, V Douglas Browning, and Howard M Taylor. “Stem diameter in relation to plant water status”. In: *Plant Physiology* 48 (Dec. 1971), pp. 683–685. DOI: 10.1104/pp.48.6.683.
- [6] Kazumasa Wakamori and Hiroshi Mineno. “Optical flow-based analysis of the relationships between leaf wilting and stem diameter variations in tomato plants”. In: *Plant Phenomics* 2019 (Oct. 2019). DOI: 10.34133/2019/9136298.
- [7] Francisco M Padilla et al. “Proximal optical sensors for nitrogen management of vegetable crops: A review”. In: *Sensors* 18 (June 2018), p. 2083. DOI: 10.3390/s18072083.
- [8] Salvadore J Locascio et al. “Nitrogen and potassium application scheduling effects on drip-irrigated tomato yield and leaf tissue analysis.” In: *HortScience* 32 (Apr. 1997), pp. 230–235. DOI: 10.21273/HORTSCI.32.2.230.
- [9] Robert R Coltman. “Yields of greenhouse tomatoes managed to maintain specific petiole sap nitrate levels”. In: *HortScience* 23 (Feb. 1988), pp. 148–151. DOI: 10.21273/HORTSCI.23.1.148.
- [10] Francesco Tei, Paolo Benincasa, and Marcello Guiducci. “Critical nitrogen concentration in processing tomato”. In: *European Journal of Agronomy* 18.1-2 (2002), pp. 45–55. DOI: 10.1016/S1161-0301(02)00096-5.
- [11] Daniel Marc G dela Torre, Jay Gao, and Cate Macinnis-Ng. “Remote sensing-based estimation of rice yields using various models: A critical review”. In: *Geo-spatial Information Science* 24 (Oct. 2021), pp. 580–603. DOI: 10.1080/10095020.2021.1936656.
- [12] A Cartelat et al. “Optically assessed contents of leaf polyphenolics and chlorophyll as indicators of nitrogen deficiency in wheat (*Triticum aestivum* L.)” In: *Field Crops Research* 91 (Jan. 2005), pp. 35–49. DOI: 10.1016/j.fcr.2004.05.002.
- [13] Francisco M Padilla et al. “Monitoring nitrogen status of vegetable crops and soils for optimal nitrogen management”. In: *Agricultural Water Management* 241 (Nov. 2020), p. 106356. DOI: 10.1016/j.agwat.2020.106356.
- [14] FM Padilla et al. “Threshold values of canopy reflectance indices and chlorophyll meter readings for optimal nitrogen nutrition of tomato”. In: *Annals of Applied Biology* 166 (Mar. 2015), pp. 271–285. DOI: 10.1111/aab.12181.
- [15] Anant Bahadur, TD Lama, SNS Chaurasia, et al. “Gas exchange, chlorophyll fluorescence, biomass production, water use and yield response of tomato (*Solanum lycopersicum*) grown under deficit irrigation and varying nitrogen levels”. In: *Indian J. Agric. Sci* 85 (2015), pp. 224–228. DOI: 10.56093/ijas.v85i2.46506.

- [16] Zheyuan Xiao et al. “Relationship between the dynamic characteristics of tomato plant height and leaf area index with yield, under aerated drip irrigation and nitrogen application in greenhouses”. In: *Agronomy* 13.1 (2022), p. 116. DOI: 10.3390/agronomy13010116.
- [17] Solomon O Olagunju et al. “Effect of NPK fertiliser on upper and basal stem diameters and implication on growth habit of tomato”. In: *Journal of the Saudi Society of Agricultural Sciences* 23.1 (2024), pp. 55–66. DOI: 10.1016/j.jssas.2023.09.002.
- [18] G Gianquinto et al. “A methodological approach for defining spectral indices for assessing tomato nitrogen status and yield”. In: *European Journal of Agronomy* 35 (Oct. 2011), pp. 135–143. DOI: 10.1016/j.eja.2011.05.005.
- [19] Hyrum B Johnson. “Plant pubescence: An ecological perspective”. In: *The Botanical Review* 41 (July 1975), pp. 233–258. DOI: 10.1007/BF02860838.
- [20] Shuichi Kinoshita and Shinya Yoshioka. “Structural Colors in Nature: The Role of Regularity and Irregularity in the Structure”. In: *ChemPhysChem* 6 (Aug. 2005), pp. 1442–1459. DOI: 10.1002/cphc.200500007.
- [21] Rox Middleton et al. “Self-assembled, disordered structural color from fruit wax bloom”. In: *Science Advances* 10 (Feb. 2024). DOI: 10.1126/sciadv.adk4219.
- [22] Katherine R Thomas et al. “Function of blue iridescence in tropical understorey plants”. In: *Journal of The Royal Society Interface* 7 (Dec. 2010), pp. 1699–1707. DOI: 10.1098/rsif.2010.0201.
- [23] JD Barbour, RR Farrar Jr, and GG Kennedy. “Interaction of fertilizer regime with host-plant resistance in tomato”. In: *Entomologia Experimentalis et Applicata* 60 (Sept. 1991), pp. 289–300. DOI: 10.1111/j.1570-7458.1991.tb01549.x.
- [24] Ellis Hoffland et al. “Nitrogen Availability and Defense of Tomato Against Two-spotted Spider Mite”. In: *Journal of Chemical Ecology* 26 (Dec. 2000), pp. 2697–2711. DOI: 10.1023/A:1026477423988.
- [25] Richard T Wilkens et al. “Resource availability and the trichome defenses of tomato plants”. In: *Oecologia* 106 (Apr. 1996), pp. 181–191. DOI: 10.1007/BF00328597.
- [26] Nick Bergau et al. “The development of type VI glandular trichomes in the cultivated tomato *Solanum lycopersicum* and a related wild species *S. habrochaites*”. In: *BMC Plant Biology* 15 (Dec. 2015), p. 289. DOI: 10.1186/s12870-015-0678-z.
- [27] Qinglin Li et al. “The effects of nitrogen on micro-structure of tomato leaf”. In: *2014 ASABE Annual International Meeting*. July 2014. DOI: 10.13031/aim.20141912263.
- [28] GLD Leite et al. “Effect of fertilization levels, age and canopy height of *Lycopersicon hirsutum* on the resistance to *Myzus persicae*”. In: *Entomologia Experimentalis et Applicata* 91 (May 1999), pp. 267–273. DOI: 10.1046/j.1570-7458.1999.00493.x.
- [29] Zhong Qiu Zhao et al. “Object Detection With Deep Learning: A Review”. In: *IEEE Transactions on Neural Networks and Learning Systems* 30 (Nov. 2019), pp. 3212–3232. DOI: 10.1109/TNNLS.2018.2876865.
- [30] Luc Vincent and Pierre Soille. “Watersheds in digital spaces: an efficient algorithm based on immersion simulations”. In: *IEEE Transactions on Pattern Analysis and Machine Intelligence* 13 (June 1991), pp. 583–598. DOI: 10.1109/34.87344.
- [31] Jorge Mendes et al. “Smartphone Applications Targeting Precision Agriculture Practices—A Systematic Review”. In: *Agronomy* 10 (May 2020), p. 855. DOI: 10.3390/agronomy10060855.
- [32] Marion Neumann et al. “Erosion Band Features for Cell Phone Image Based Plant Disease Classification”. In: *2014 22nd International Conference on Pattern Recognition*. Aug. 2014, pp. 3315–3320. DOI: 10.1109/ICPR.2014.571.

- [33] Azeddine Elhassouny and Florentin Smarandache. “Smart mobile application to recognize tomato leaf diseases using Convolutional Neural Networks”. In: *2019 International Conference of Computer Science and Renewable Energies (ICCSRE)*. July 2019, pp. 1–4. DOI: 10.1109/ICCSRE.2019.8807737.
- [34] Zheng Li et al. “Non-invasive plant disease diagnostics enabled by smartphone-based fingerprinting of leaf volatiles”. In: *Nature Plants* 5 (Aug. 2019), pp. 856–866. DOI: 10.1038/s41477-019-0476-y.
- [35] Jürgen Münch et al. “Creating Minimum Viable Products in Industry-Academia Collaborations”. In: *Lean Enterprise Software and Systems: 4th International Conference, LESS 2013, Galway, Ireland, December 1-4, 2013, Proceedings*. Dec. 2013, pp. 137–151. DOI: 10.1007/978-3-642-44930-7_9.
- [36] Eric Ries. *The Lean Startup*. en. New York, NY: Crown Publishing Group, Oct. 2011.
- [37] Intel Corporation and Willow Garage Inc. *OpenCV-contrib-python*. https://github.com/opencv/opencv_contrib. Version 4.6.0.66.
- [38] James Anthony Seibert, John M Boone, and Karen K Lindfors. “Flat-field correction technique for digital detectors”. In: *Medical Imaging 1998*. Vol. 3336. July 1998, pp. 348–354. DOI: 10.1117/12.317034.
- [39] Joris J Glas et al. “Plant Glandular Trichomes as Targets for Breeding or Engineering of Resistance to Herbivores”. In: *International Journal of Molecular Sciences* 13 (Nov. 2012), pp. 17077–17103. DOI: 10.3390/ijms131217077.
- [40] Philip J Clark and Francis C Evans. “Distance to Nearest Neighbor as a Measure of Spatial Relationships in Populations”. In: *Ecology* 35 (Oct. 1954), pp. 445–453. DOI: 10.2307/1931034.
- [41] Steven S Skiena. *The algorithm design manual*. Vol. 2. Springer, 1998. DOI: 10.5555/1410219.
- [42] Pdraig Cunningham and Sarah Jane Delany. “k-Nearest Neighbour Classifiers - A Tutorial”. In: *ACM Computing Surveys* 54 (July 2022), pp. 1–25. DOI: 10.1145/3459665.
- [43] Dennis Robert Hoagland and Daniel Israel Arnon. “The water-culture method for growing plants without soil.” In: (1938).
- [44] Roberto S Velazquez-Gonzalez et al. “A Review on Hydroponics and the Technologies Associated for Medium- and Small-Scale Operations”. In: *Agriculture* 12 (Mar. 2022), p. 646. DOI: 10.3390/agriculture12050646.
- [45] Y Ishihara, H Hitomi, and Y Yamaki. “Effect of Composition of an Improved Nutrient Solution for a Closed Hydroponic System on Nutrient Absorption by Tomatoes”. In: *Horticultural Research (Japan)* 6 (July 2007), pp. 391–397. DOI: 10.2503/hrj.6.391.
- [46] Ronald Aylmer Fisher et al. *The design of experiments*. Vol. 21. Springer, 1966.
- [47] Python Software Foundation. *Python*. <https://www.python.org>. Version 3.10.9.final.0.
- [48] scikit-learn-contrib. *imbalanced-learn*. <https://github.com/scikit-learn-contrib/imbalanced-learn>. Version 0.12.0.
- [49] K.Guolin and Microsoft Research. *LightGBM*. <https://github.com/microsoft/LightGBM>. Version 3.3.5.
- [50] S.Lundberg and S. Lee. *SHAP*. <https://github.com/slundberg/shap>. Version 0.43.0.
- [51] S.Ianaré. *ExifRead*. <https://github.com/ianare/exif-py>. Version 3.0.0.
- [52] Alain F Zuur, Elena N Ieno, and Chris S Elphick. “A protocol for data exploration to avoid common statistical problems”. In: *Methods in Ecology and Evolution* 1 (Mar. 2010), pp. 3–14. DOI: 10.1111/j.2041-210X.2009.00001.x.

- [53] Mehryar Mohri, Afshin Rostamizadeh, and Ameet Talwalkar. *Foundations of Machine Learning*. 2nd ed. Adaptive Computation and Machine Learning series. Cambridge, MA: The MIT Press, 2018.
- [54] Guo Haixiang et al. “Learning from class-imbalanced data: Review of methods and applications”. In: *Expert Systems with Applications* 73 (May 2017), pp. 220–239. DOI: 10.1016/j.eswa.2016.12.035.
- [55] Nitesh V Chawla et al. “SMOTE: Synthetic Minority Over-sampling Technique”. In: *Journal of Artificial Intelligence Research* 16 (June 2002), pp. 321–357. DOI: 10.1613/jair.953.
- [56] Guolin Ke et al. “LightGBM: a highly efficient gradient boosting decision tree”. In: *Advances in neural information processing systems* 30 (2017).
- [57] Mohammad Hossin and Md Nasir Sulaiman. “A review on evaluation metrics for data classification evaluations”. In: *International journal of data mining & knowledge management process* 5 (Mar. 2015), pp. 01–11. DOI: 10.5121/ijdkp.2015.5201.
- [58] László A Jeni, Jeffrey F Cohn, and Fernando De La Torre. “Facing Imbalanced Data—Recommendations for the Use of Performance Metrics”. In: (Sept. 2013), pp. 245–251. DOI: 10.1109/ACII.2013.47.
- [59] Scott M Lundberg and Su-In Lee. “A Unified Approach to Interpreting Model Predictions”. In: *Advances in neural information processing systems* 30 (2017), pp. 4768–4777.
- [60] Fidel Maureira, Kirti Rajagopalan, and Claudio O Stöckle. “Evaluating tomato production in open-field and high-tech greenhouse systems”. In: *Journal of Cleaner Production* 337 (Feb. 2022), p. 130459. DOI: 10.1016/j.jclepro.2022.130459.
- [61] Donald E Farrar and Robert R Glauber. “Multicollinearity in regression analysis: the problem revisited”. In: *The Review of Economic and Statistics* (1967), pp. 92–107. DOI: 10.2307/1937887.
- [62] David J Glass and Ned Hall. “A brief history of the hypothesis”. In: *Cell* 134.3 (2008), pp. 378–381. DOI: 10.1016/j.cell.2008.07.033.